The Role of Surface Fluxes in MJO Propagation through the Maritime Continent

JUSTIN HUDSON[a] AND ERIC MALONEY[a]

[a] *Department of Atmospheric Science, Colorado State University, Fort Collins, Colorado*

(Manuscript received 30 June 2022, in final form 14 October 2022)

ABSTRACT: The "barrier effect" of the Maritime Continent (MC) is a known hurdle in understanding the propagation of the Madden–Julian oscillation (MJO). To understand the differing dynamics of MJO events that propagate versus stall over the MC, a new tracking algorithm utilizing 30–96-day-filtered NOAA Interpolated OLR anomalies is presented. Using this algorithm, MJO events can be identified, tracked, and described in terms of their propagation characteristics. Latent heat flux from OAFlux and CYGNSS surface winds and fluxes are compared for MJO events that do and do not propagate through the MC. Events that successfully propagate through the MC demonstrate regional surface flux anomalies that are stronger, more spatially coherent, and have a larger fetch. The spatial scale of convective anomalies for events that successfully propagate through the MC region is also larger than for terminating events. Large-scale enhancement of latent heat fluxes near and to the east of the date line, equally driven by dynamic and thermodynamic effects, also accompanies MJO events that successfully propagate through the MC. These findings are placed in the context of recent theoretical models of the MJO in which latent heat fluxes are important for propagation and destabilization.

KEYWORDS: Maritime Continent; Madden-Julian oscillation; Surface fluxes

1. Introduction

The Madden–Julian Oscillation (MJO; Madden and Julian 1971, 1972) is a tropical intraseasonal (30-90-day) oscillation maximizing in amplitude in boreal winter that propagates eastward along the equator. The classical picture of the MJO is that of a large-scale enhanced precipitation region zonally bound by suppressed precipitation that propagates from the Indian Ocean (IO), through the Maritime Continent (MC), and then into the Pacific Ocean where it dissipates. The spatial scale of the MJO precipitation envelope is of zonal wavenumber 1–3 (Wheeler and Kiladis 1999). The MJO is also coupled to a large-scale anomalous circulation at 200 and 850 hPa that spans much of the tropics and can modulate tropical cyclone activity (e.g., Maloney and Hartmann 2000).

The influence of the MJO extends beyond the Indo-Pacific warm pool, with MJO teleconnections impacting regions across the globe (Arcodia et al. 2020; Barnes et al. 2019; Lee and Seo 2019; Zhou et al. 2012). For example, the MJO produces Rossby wave teleconnections to the extratropics that impact atmospheric river activity along the West Coast of the United States (e.g., Guan and Waliser 2015). The MJO plays an important role in forecasting skill on subseasonal-to-seasonal (S2S) time scales in the midlatitudes given these global teleconnections (Baggett et al. 2017; Nardi et al. 2020). As an example, through Rossby wave breaking the MJO can induce blocking of the jet stream over Europe increasing the chance for severe weather (Henderson et al. 2016). The inability of forecasting models to properly simulate MJO propagation across the MC has negative implications for S2S forecast skill in western North America and other regions (e.g., Hsiao et al. 2022) potentially increasing both loss of life and economic damage. Inability of climate models to simulate the MJO also has potentially important implications for simulation of lower-frequency tropical variability such as El Niño–Southern Oscillation (ENSO), since wind bursts associated with MJO events can initiate El Niño warm events through forcing of downwelling oceanic Kelvin waves (e.g., McPhaden 1999).

Despite the importance of the MJO for climate, extreme events, and subseasonal prediction, many unanswered questions remain about its formation, maintenance, and propagation (Jiang et al. 2020; Zhang 2005). One mystery surrounding the MJO is known as the "barrier effect" of the MC (Salby and Hendon 1994; Zhang and Ling 2017). A sizable fraction of MJO events fail to propagate through or weaken over the MC region (Ling et al. 2019). Those that do make their way through the MC region tend to detour south of the island of Java (Wu and Hsu 2009). The MC produces too much of a barrier to MJO propagation in many global models (Inness and Slingo 2006), which negatively affects the ability of models to predict the MJO (e.g., Kim et al. 2014). A variety of processes are hypothesized to affect MJO propagation across the MC, including a prior strong dry anomaly in the west Pacific (Kim et al. 2014), the diurnal cycle over MC islands (Zhang and Ling 2017), westward-propagating Rossby waves in the west Pacific (DeMott et al. 2018), air–sea coupling (Hirata et al. 2013), and competing westward-propagating intraseasonal modes (e.g., Gonzalez and Jiang 2019). Jiang et al. (2020) provides an extensive summary of many of these hypothesized processes. Recent studies with CMIP6 models suggest that MJO propagation through the MC may be improved in the most recent generation of climate models (e.g., Ahn et al. 2020), a result they attribute to improved mean-state horizontal moisture gradients in the MC region and their impact on horizontal moisture advection.

Corresponding author: Justin Hudson, justin.hudson@colostate.edu

DOI: 10.1175/JCLI-D-22-0484.1

This paper will explore the possibility that surface flux variability helps to maintain MJO propagation through the MC. Variations in latent heat flux (LHF) have been hypothesized to play a critical role in maintaining and guiding the propagation of the MJO, but the exact mechanism for how LHF supports the MJO is still a matter of debate (Bui et al. 2020; DeMott et al. 2014, 2015; Emanuel 2020; Fuchs and Raymond 2017; Khairoutdinov and Emanuel 2018; Maloney 2009; Raymond and Fuchs 2018; Riley Dellaripa and Maloney 2015; Sentić et al. 2020; Sobel and Maloney 2012; Wolding and Maloney 2015).

Two major recent bodies of theory suggest the importance of wind-induced surface fluxes for MJO maintenance and propagation, and will guide the investigations here. The first is moisture mode theory (e.g., Adames and Kim 2016; Sobel and Maloney 2012, 2013). Assuming weak tropical temperature gradients, moisture mode theory argues that processes regulating the evolution of the tropical moisture field, which then modulates precipitation, are essential to the dynamics of the MJO. Some studies have argued that longwave cloud radiative feedbacks, which can attain a magnitude of 20% of MJO precipitation anomalies (when these anomalies are expressed in W m^{-2}), modulate the moisture budget to support MJO convection. Radiative anomalies are balanced by adiabatic cooling anomalies in the thermodynamic energy equation, with the associated vertical velocity providing a vertical moisture advection (Wolding et al. 2016). Other studies have argued that surface flux feedbacks, largely wind-driven, can also support MJO moisture anomalies that support convection (Araligidad and Maloney 2008; Bui et al. 2020; DeMott et al. 2016). In particular, a collocation between latent heat flux anomalies and the same signed precipitation anomalies helps to support the column moisture field that supports MJO precipitation anomalies. We hypothesize that surface flux anomalies help to support MJO convective events that propagate through the MC. Kang et al. (2022) suggests that the westerly mean-state surface winds in the MC during boreal winter create a positive surface flux feedback, in support of this hypothesis. A key aspect of this investigation is the strength, coherence, and spatial scale of local LHF anomalies driven by MJO perturbation winds relative to MJO precipitation anomalies in the MC region, especially when compared to the strength of OLR anomalies versus precipitation, as radiative feedbacks have previously been shown to help maintain MJO convection (Adames and Kim 2016). Such comparisons allow for a greater understanding of the relative importance of these LHF anomalies to OLR anomalies in MJO maintenance and propagation. This might help guide efforts to improve the simulation of the MJO in models, since model surface flux anomalies associated with tropical disturbances are dependent on not only model parameterizations, but also factors such as model basic state winds that determine the sign of flux anomalies given a vector wind anomaly.

Another body of theory, referred to as wind-induced surface heat exchange (WISHE), argues that enhanced surface fluxes to the east of MJO convection help to support eastward MJO propagation in the presence of mean tropical easterly low-level winds (Emanuel 1987; Raymond and Fuchs 2018; Sentić et al. 2020). We also hypothesize that MJO events that propagate across the MC are associated with a stronger enhanced LHF signal in the central and eastern Pacific than nonpropagating events. Both groups of theory place LHF as a key underpinning to how the MJO maintains itself; to this end, moisture mode theory relies on surface fluxes working in tandem with radiative feedbacks to enhance moist static energy (MSE) anomalies locally, in contrast to the singular importance WISHE places on wind-driven fluxes to the east of the MJO for controlling propagation.

Some studies to address MJO propagation through the MC have involved the use of indices based on empirical orthogonal function (EOF) analysis. Attempts to understand and predict the MJO using indices such as the Real-time Multivariate MJO Index (RMM; Wheeler and Hendon 2004) and the outgoing longwave radiation (OLR)-based MJO Index (OMI; Kiladis et al. 2014) have involved breaking the MJO down into eight phases based on the broad geographic location of the MJO's enhanced convective phase. While these indices have allowed for greater insight into MJO dynamics, they limit our understanding of exactly where the MJO's enhanced convective region is at any time. Another approach to understanding MJO propagation relies on using tracking algorithms to identify and track MJO convective events, improving localization of the MJO convective center. Precipitation tracking has been shown to identify and locate MJO events providing information about MJO propagation as well as the MC "barrier effect" (Kerns and Chen 2016, 2020; Ling et al. 2019; Zhang and Ling 2017). Kerns and Chen (2016, 2020) used spatially smoothed 72-h accumulated precipitation to track large-scale (>300 000 km^2) convective regions, and found that the RMM index did not agree with their tracking on the presence of an MJO event by either lacking an MJO signal during a period where they tracked a precipitation event, or by producing a signal when there was no identified MJO event.

Singh and Kinter (2020) showed that intraseasonally filtered OLR anomalies combined with a multiple object tracking algorithm are capable of identifying and tracking several classes of tropical intraseasonal oscillations. Both Kerns and Chen (2016, 2020) and Singh and Kinter (2020) showed that direct identification and tracking methods are capable of highlighting key regional and global features for different categories of MJO events such as the relationship to the state of the ENSO (Kerns and Chen 2016, 2020), and how seasonality of moisture, low-level circulation, and sea surface temperature (SST) control MJO propagation (Singh and Kinter 2020).

Here, we develop a tracking technique that is inspired by that of Singh and Kinter (2020) and Kerns and Chen (2016, 2020), and use it to understand the role of surface heat flux anomalies for MJO propagation through the MC region. Filtered OLR anomalies allow for a robust and coherent MJO identification technique for tracking, which can be used to diagnose the importance of surface flux feedbacks to MJO dynamics in the MC, and help explain why some events propagate through the MC, and others terminate. In section 2 we outline the specifics of our algorithm, as well as the data used to investigate the dynamics of MJO propagation and maintenance. In section 3, our method is used to assess the

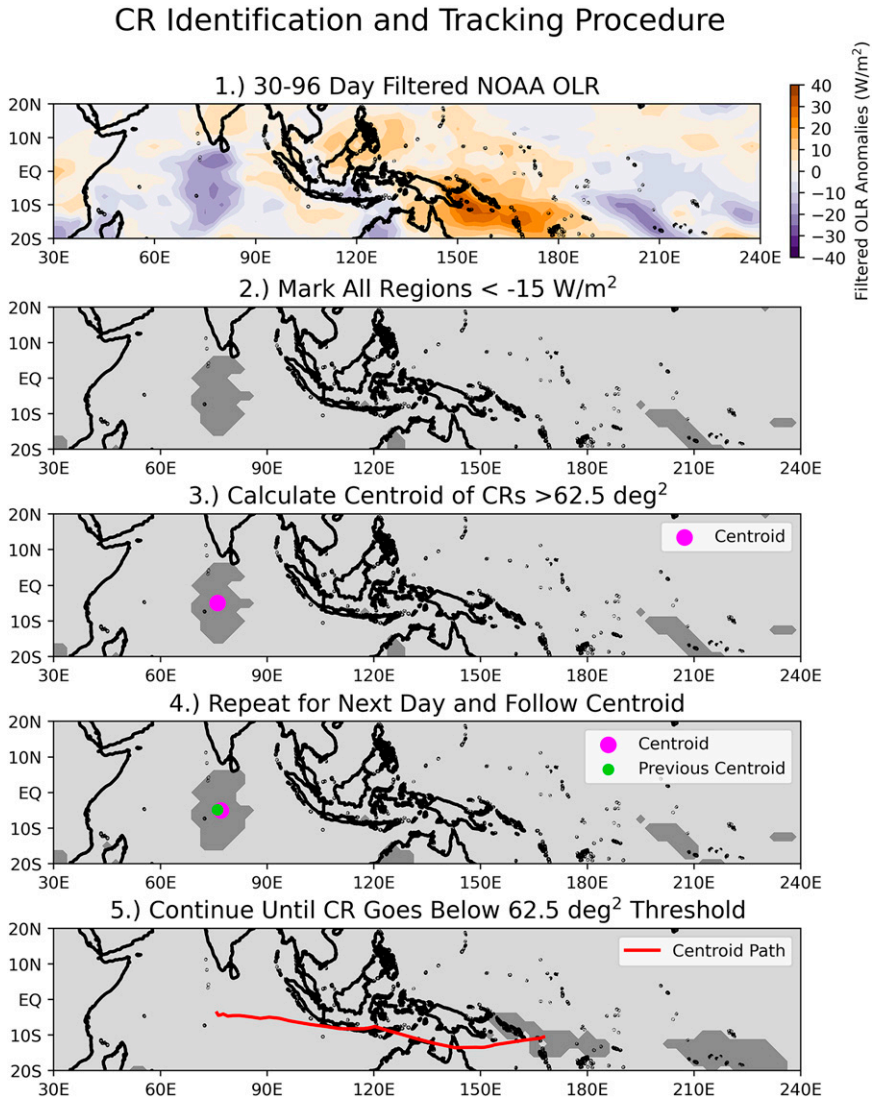

FIG. 1. A schematic view of how our tracking algorithm works. Intraseasonally filtered NOAA interpolated OLR data are used (step 1) and produce binary maps to highlight regions with anomalies less than -15 W m^{-2} (step 2). The algorithm then identifies regions greater than a specified size threshold (step 3) and follows them as they propagate through time storing the position of the geometric centroid of the region on each day (step 5). Using this, the path taken by a specified MJO event can be reconstructed as it propagates (step 5).

importance of surface flux feedbacks to MJO maintenance and propagation through the MC region. In section 4 we discuss our results in the context of current theories of MJO propagation, and in section 5 we present conclusions.

2. Methodology and data

a. OLR tracking algorithm

Interpolated daily mean OLR data from 1985 to 2020 on a 2.5° × 2.5° grid provided by the National Oceanic and Atmospheric Administration (NOAA) Office of Oceanic and Atmospheric Research (OAR) Earth Systems Research Laboratory (ESRL) Physical Sciences Laboratory (PSL), Boulder Colorado, USA, from their website (https://psl.noaa.gov/data/gridded/data.olrcdr.interp.html) was used to diagnose the location of convection (Liebmann and Smith 1996). To do this, the 30-yr daily mean OLR (1981–2010) provided alongside the interpolated OLR data was subtracted gridwise producing daily anomalies relative to the 30-yr mean. The calculated anomalies were then filtered to isolate MJO time scale signals using a 30–96-day bandpass filter with a Hanning window (step 1 in Fig. 1). The OLR data were subsetted to the Indo-Pacific warm pool region (20°N–20°S, 30°–240°E) where the MJO shows its strongest convective variability during boreal winter.

To highlight regions of enhanced intraseasonal convection, binary maps were produced whereby grid cells of filtered

OLR anomalies less than -15 W m^{-2} [similar to that of Singh and Kinter (2020)], indicating strong convection, were given a value of 1 and all other grid cells were given a value of 0. Our results are not qualitatively sensitive to varying this threshold between -10 and -20 W m^{-2} (step 2 in Fig. 1). These binary maps allow for an easily searchable space where regions of intraseasonal convection can be quickly identified.

The tracking algorithm works by first searching the produced binary maps for areas of enhanced convection. The algorithm then utilizes eight-connectivity (the fact that any point in 2D space has eight neighboring points) to map these regions, and we henceforth refer to these as convective regions (CRs) (step 3 in Fig. 1). Because MJO convective anomalies have a large spatial scale (Wheeler and Kiladis 1999), tracking was limited to CRs above a certain size threshold of 10 pixels (62.5 deg^2 on a 2.5° × 2.5° grid, or 770 000 km^2 in the tropics). Sensitivity to this threshold is low between 10 and 15 pixels. Lowering the size threshold from 10 to 5 pixels has little impact on the number of events that propagate through the MC but does increase the number of small CRs that propagate only over the Indian Ocean. Only CRs above our size threshold of 10 pixels were tracked. If a CR fell below this threshold the tracked event was considered to have dissipated. Details on how we handle CRs that temporarily fall below this threshold are described later in this section.

From theory and observations, we know that relative to its spatial scale, the propagation speed of the MJO is quite slow (Madden and Julian 1972; Adames and Kim 2016). Leveraging this fact, once the algorithm has identified all the CRs on day N it then compares the grid points within each tracked CR against the grid points of CRs on day $N - 1$. Using the points within CRs on days N and $N - 1$, the two CRs can be connected using a similarity threshold where the sum of grid points in the CR on day N that are found in the CR on day $N - 1$ are divided by the number of grid points in the CR on day N (step 4 in Fig. 1). This was set to a value of 0.2, meaning that 20% of points must be similar. This is different from the approach of Singh and Kinter (2020) who used a Kalman filter to predict the location of a tracked event on a subsequent day and searched in a specified radius around the predicted location. This overlapping points methodology was used by Kerns and Chen (2016, 2020) although their threshold was set to 50% of points overlapping. We found that our results are not sensitive to this value unless set to very low or very high values. This process is repeated for all days from 1 October 1985 to 31 May 2020 and is agnostic to where CRs originate, dissipate, and the direction and speed of their propagation (step 5 in Fig. 1). This minimizes issues such as when the center of convection temporarily stalls or moves westward on an individual day. Refinement to only events displaying MJO-specific characteristics is done posttracking.

Previous tracking studies have shown that the path of individual MJO events, while generally moving eastward, can be complicated, and that for a tracking algorithm to be robust it must account for tracked regions that overlap or split into multiple regions (Kerns and Chen 2016, 2020; Singh and Kinter 2020). To handle such variability our algorithm loops over the list of all tracked CRs to connect any events that may have been disrupted, temporarily fallen below a size or convective threshold, and other complex behavior. To accomplish this our algorithm draws a 75°-wide (37.5° to the east and west) and 15°-tall (7.5° to the north and south) box around the last known geometric centroid for a CR. If there is another tracked CR in that box within 15 days of when the CR dissipated (5 days before and 10 days after), which persists for at least 2 days, the algorithm considers the two events to be connected and combines them into a singular event. By looking up to 10 days after when a CR dissipates, we can better account for the 'jump' MJO events of Wang et al. (2019) that dissipate and reform on the far side of the MC approximately 3–8 days later. Changing the algorithm to only consider 5 days before and after a CR dissipates does not qualitatively change our results. If there are multiple CRs the algorithm ranks the possible CRs to connect to by similarity of angle of propagation and distance. Ties in ranking are decided with the closest CR being chosen.

Tracked CRs are also capable of splitting into multiple convective regions. To handle this the algorithm looks at a list of all CRs that meet the similarity threshold on day N for a CR on day $N - 1$. If there are multiple CRs the algorithm chooses the largest CR to be the continuation of the CR on day $N - 1$ and any remaining CRs are marked as new events to be tracked. Given our chosen parameters a CR splitting into multiple regions that still met the similarity threshold occurs for 62.9% of all tracked events.

Another possible behavior is that CRs can merge. If multiple CRs on day $N - 1$ match (meet our overlapping-point threshold) to a singular CR on day N the algorithm looks at the CRs on day $N - 1$, and whichever CR is the oldest (having been tracked for the most days) is considered to be the main progenitor of the combined CR. The combined CR will inherit the tracking data from the oldest CR on day $N - 1$ and the remaining CRs will be marked as terminated and tracking ceased. This merging or overlapping behavior is quite common and occurs for 16.5% of all tracked events.

As CRs are connected between days, a record of each CR's position (determined by its geometric centroid), size, and meridional and zonal velocity between frames is produced. The resulting database can be refined based on any of those statistics to further limit the results to MJO events of specific characteristics. By focusing on events that originate in the IO and propagate through the MC we can identify events that are likely to be classic boreal winter MJO events. Figure 1 shows a schematic view of the tracking process for an individual boreal winter MJO event.

Inspired by the results and methodology from previous studies such as Kerns and Chen (2016, 2020) and Singh and Kinter (2020), only CRs that met the following criteria were considered to be MJO events:

1) The size must be greater than 10 pixels (62.5 deg^2).
2) Tracking must cease at least 30° east of where MJO events initiate.
3) The entire event must occur during 'boreal winter' (1 October–31 May) to focus on predominantly eastward-propagating MJO events. No events we considered to be

MJOs in our final sample had their tracking ceased due to this cutoff.

4) To further omit BSISO events, tracking must not end 15° or more north from where it initiated and tracking cannot end north of 15°N.
5) The tracking initiation longitude must be west of 115°E, given our interest in MJO propagation across the MC.
6) The terminating longitude must be east of 100°E.
7) The CR must last for at least 10 days.

All CRs that met these criteria were considered to be MJO events. Events below will also be partitioned into those that propagate through versus terminate in the MC region, as defined later.

b. Data products

Latent heat flux (LHF), 2-m specific humidity, sea surface temperature (SST), and 10-m winds from Objective Analyzed Air-Sea Fluxes (OAFLUX; Yu and Weller 2007) for the Global Oceans supported by NOAA's Global Ocean Monitoring and Observing (GOMO) Program and National Aeronautic and Space Administration's (NASA) Making Earth-System data records for Use in Research Environments (MEaSUREs) Program were acquired from Woods Hole Oceanographic Institute. These data are obtained on a 1° × 1° grid, and are available from 1985 to 2021.

Hourly Level 3 (L3) Cyclone Global Navigation Satellite System (CYGNSS) Science Data Record (SDR) v3.1 surface wind speed (Gleason et al. 2022; Pascual et al. 2021; Ruf et al. 2016, 2019) were acquired from NASA Jet Propulsion Laboratory's (JPL) Physical Oceanography Distributed Active Archive Center (PODAAC). CYGNSS is a constellation of eight satellites that retrieve wind speed based on characteristics of the forward scattered GPS signals from the ocean surface (Gleason et al. 2022). We used the "fully developed seas" version of CYGNSS. The fully developed sea version of CYGNSS assumes that the surface sea state is in equilibrium with the surface wind field. The SDR v3.1 surface winds are available from 2018 to the present. To match with OAFLUX the CYGNSS SDR v3.1 winds were converted to a daily mean value and conservatively regridded to a 1° × 1° grid using the methodology of Jones (1999).

We also acquired Level 2 (L2) Climate Data Record (CDR) v1.1 LHFs (Crespo et al. 2019) from the PODAAC that are available from 2017 to the present. CDR v1.1 LHFs were converted to a 1° × 1° grid following the algorithm described in Ruf (2018). These fluxes were produced from CYGNSS wind retrievals utilizing observational and reanalysis estimates of temperature and humidity (Crespo et al. 2019). Linear interpolation in space and time was used to fill in any gaps in the data.

Daily Integrated Multi-satellitE Retrievals for GPM (IMERG) precipitation data on a 0.1° × 0.1° grid for 2000–20 (Huffman et al. 2019) were acquired from Goddard Earth Science's Data and Information Services Center (GES DISC). IMERG combined microwave and IR precipitation estimates from satellites with other techniques such as precipitation gauge measurements to provide high-quality global precipitation estimates. To match with other datasets IMERG precipitation was conservatively regridded onto a 1° × 1° grid using the methodology of Jones (1999).

Daily 1000-hPa zonal winds from the European Centre for Medium-Range Weather Forecasts (ECMWF) fifth-generation atmospheric reanalysis (ERA5) (Hersbach et al. 2020) were obtained from the Copernicus Climate Change Service (C3S; Copernicus Climate Change Service C3S 2017) on a 0.25° × 0.25° grid for 10°N–10°S for 1979–2020. Daily 850-hPa winds from ERA5 were also obtained on a 0.25° × 0.25° grid for 25°N–25°S and 30°–240°E. ERA5 provides high-spatial-resolution and high-temporal-resolution global coverage and is the successor to ERA-Interim (ERA-I). All data were converted to daily anomalies and then filtered using the same 30–96-day bandpass filter with a Hanning window as the NOAA Interpolated OLR data, except for 1000-hPa zonal wind data that were used to assess the background wind field during MJO events.

c. Bootstrapping experiment

To test our results for statistical significance a bootstrapping experiment was carried out. To do this, for all MJO events that made it into our final sample, we kept the tracking data of the event and the length of the event in days.

Random start dates during boreal winter between 1985 and 2019 were chosen to generate synthetic events, with events not going past 31 May. Combining this with the tracking data allows us to construct synthetic events on random dates that have the same propagation path and temporal length as the observed events. For both terminating and persisting events, 5000 different synthetic composites were generated by drawing events from random dates. These composites reflect the same propagation characteristics as our observed composites and the same number of individual persisting or terminating events, but generated using random start dates.

The 5000 synthetic MJO composites form a distribution against which to compare our observed composites. Data from the observed composites were compared against the distribution produced by the synthetic composites to identify regions that are statistically significant at the 95% confidence level. The stippling in Figs. 7–11 indicates the regions identified as statistically significant.

3. Observational results

a. OAFlux results

1) BASIC TRACK BEHAVIOR

Using the settings outlined in section 2a, the tracking algorithm was applied to 35 years of 30–96-day filtered Interpolated NOAA OLR data daily anomalies, and 46 MJO events were identified. Figure 2 shows the centroid trajectories for each event as well as a heat map of tracked events.

Figure 2b shows that MJO events, when propagating into the MC region, tend to detour south of Java instead of heading eastward closer to the equator. This is expected behavior based on observations (Wu and Hsu 2009) and is a good first order check that our algorithm is identifying typical MJO event behavior. Within the MC region a less common northern

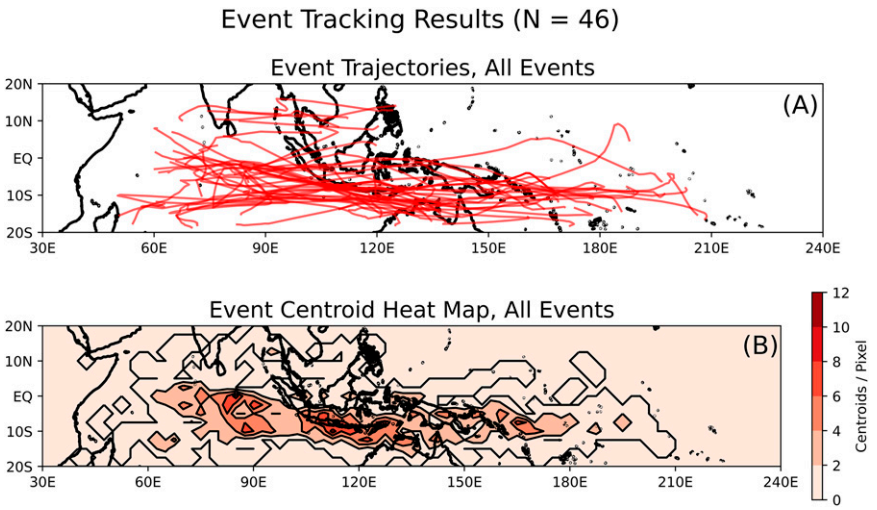

FIG. 2. (a) Individual MJO event tracks, and (b) a heat map of where MJO events prefer to propagate. Centroid tracks in (a) were smoothed using a 5-day simple moving average. For the heat map in (b), each tracked centroid was only counted once for each pixel to prevent events that stall out over the MC from being overcounted and biasing the heat maps.

propagation pathway is also apparent that goes directly over the islands of Sulawesi and New Guinea. These two propagation pathways (northern and southern) appear to reconnect near the Solomon Islands where events tend to continue propagating eastward into the equatorial Pacific. Similar density plots were produced in both Singh and Kinter (2020) as well as Kerns and Chen (2020). For Singh and Kinter (2020) these dual pathways are present and display similar behavior, yet for Kerns and Chen (2020) this behavior is missing. Events in Kerns and Chen (2020) tend to propagate directly through the MC versus detouring to the south, which may be the cause of this discrepancy. We also note that Kerns and Chen (2020) use total accumulated convective fields rather than anomalies, which may also explain some of this difference.

Kerns and Chen (2016) and Singh and Kinter (2020) both found that MJO indices do not always agree with tracking algorithms on the presence or absence of an MJO event. Dates where a tracking algorithm was actively tracking an MJO event could be marked as a weak or nonexistent MJO using various indices, and time periods demarcated by strong signals in an MJO index can have no tracked event. Given this fact, in order to compare our results against findings derived from more traditional nontracking methods, we next examined the strength of intraseasonal flux anomalies relative to precipitation by averaging over boxes in the Indian Ocean (0°–10°S, 80°–100°E), and MC (5°–15°S, 120°–140°E). This allows us to assess how important fluxes are relative to radiative feedbacks in helping to maintain the MJO in these regions, and to directly compare MJO events we identify via tracking against those in previous studies based on results from MJO indices (e.g., Bui et al. 2020).

When precipitation is expressed in watts per square meter, intraseasonal LHF anomalies have previously been found to be approximately 4%–12% of the magnitude of precipitation anomalies in the Indian Ocean and west Pacific (Bui et al. 2020; Riley Dellaripa and Maloney 2015). Unlike previous results that look broadly at the relationship between intraseasonal precipitation and flux anomalies, we only look at the relationship when MJO events are defined to exist using our algorithm (black points in Fig. 3), and also periods when the OMI index is greater than one (red points in Fig. 3). Doing this allows us to investigate the importance of this relationship for the MJO and directly compare our results against previous studies. LHF anomalies are 7%–13% the magnitude of precipitation in these boxes (Figs. 3c,d), which agrees with previous findings, and suggests that latent heat flux anomalies play an important role in helping to maintain MJO convection in the MC region in the context of moisture mode theory by supplementing the moisture budget both locally and via advection. In comparison, column longwave radiative flux anomalies as diagnosed by negative OLR anomalies are about 16%–22% of precipitation anomalies (Figs. 3a,b).

Figure 4 shows statistical information for all 46 tracked events. The mean propagation speed is 3.36 m s^{-1} (Fig. 4d) with a mean event length of 43.7 days (Fig. 4c). This propagation speed is slightly slower than what MJO observations suggest (5 m s^{-1}), but is comparable to results from some other tracking studies (Kerns and Chen 2016, 2020; Singh and Kinter 2020). It does disagree with the mean value of slightly more than 5 m s^{-1} from Zhang and Ling (2017). The discrepancy between our results and those of Zhang and Ling (2017) could be because they track the meridional mean of precipitation versus our study and those of Kerns and Chen (2016, 2020), and Singh and Kinter (2020) that track the full envelope of convection. The convective signal from the MJO using other techniques such as lag-correlation analysis has been found to be about 4 m s^{-1} in the Indo-Pacific warm pool, which is slower than the propagation of the MJO's wind signal (e.g., Maloney and Sobel 2004; CLIVAR Madden–Julian Oscillation Working Group 2009). The mean event length

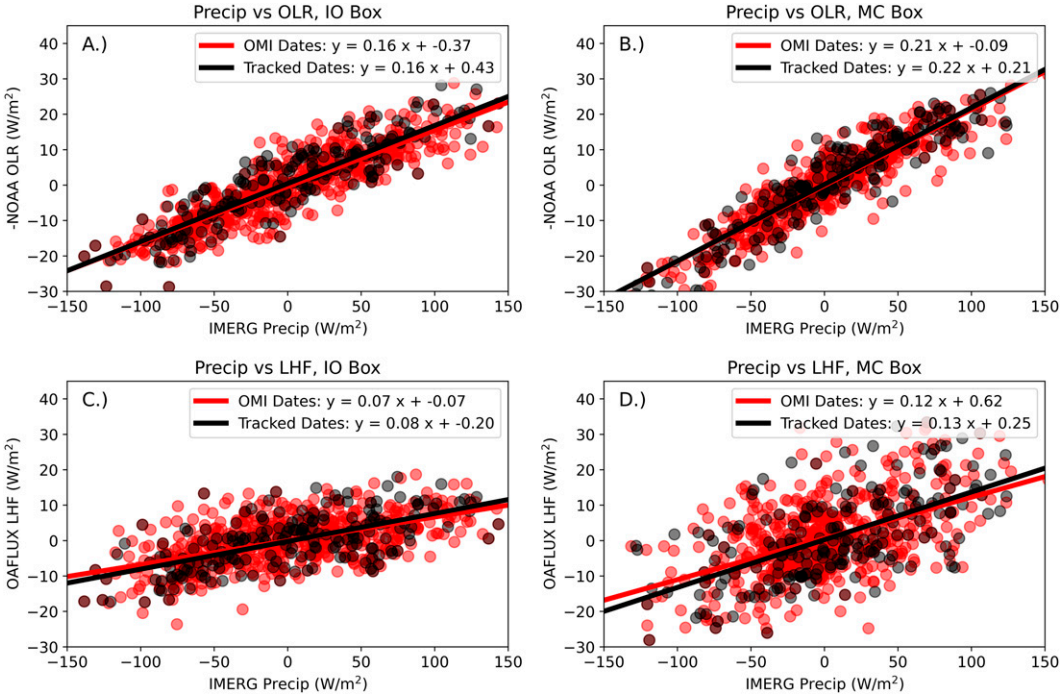

FIG. 3. Scatterplots of intraseasonal precipitation, OLR, and LHF anomalies in boxes over the (a),(c) Indian Ocean (IO Box) and (b),(d) Maritime Continent (MC Box). For purposes of comparison, IMERG precipitation has been expressed in W m^{-2}.

agrees with the results of Singh and Kinter (2020) for eastward-propagating tropical intraseasonal oscillations, and observations of the MJO that place it around 45 days (e.g., Madden and Julian 1972).

The distribution for where tracking initiates (Fig. 4a) is approximately normal and centered around 70°–80°E in the Indian Ocean. The distribution for where tracking terminates (Fig. 4b) has a bimodal appearance with a group of tracks that terminate over the MC region and another group that propagates into the Pacific Ocean. Because the two groups can be split at 150°E (roughly the eastern edge of the island of New Guinea), we refer to events where tracking ceased over the MC (100°–150°E) as "terminating" events, and events that propagate into the Pacific Ocean as "persisting" events. We define 23 persisting events and 23 terminating events with this definition, a similar ratio to that of Kerns and Chen (2016, 2020). This natural distinction between the two groups is consistent with the MC's "barrier effect," where the MJO weakens and potentially dissipates before reaching the Pacific Ocean (Ling et al. 2019; Salby and Hendon 1994; Zhang and Ling 2017).

As a first-order approach to understand why some events propagate through the MC region, we compare the tracking for both classes of events in Fig. 5. The track density panels (Figs. 5c,d) show that a large difference does not exist between the two categories in terms of where they prefer to initially propagate. Both groups start to detour south of Java, although terminating events do tend to go slightly farther south toward the northwestern coast of Australia. From these results the "barrier effect" of the MC does not appear to be generally dependent on the path by which the MJO convective disturbance originally enters the MC. Further, comparing persisting and terminating events against ENSO reveals no preference for either El Niño or La Niña, with both categories of events preferring a neutral ENSO state (not shown here). Similar comparison also reveals no preference for the state of the quasi-biennial oscillation (QBO).

2) SURFACE FLUXES AND LOCAL FEEDBACKS ONTO TERMINATING VERSUS PERSISTING EVENTS

Examination of local surface variables is conducted to provide physical insight into propagating versus nonpropagating events, viewed through the lens of moisture mode theory. The ratio of OLR and LHF anomalies to precipitation anomalies (measured in W m^{-2}) has been used in the context of moisture mode theory to better understand what role radiative feedbacks and surface flux feedbacks play in MJO maintenance and propagation (e.g., Adames and Kim 2016; Bui et al. 2020; Riley Dellaripa and Maloney 2015). To understand the evolution of these ratios along MJO tracks, a 10° latitude × 30° longitude box centered on a CR's geometric centroid was considered for every day of tracking. The spatial mean of OLR, LHF, and precipitation anomalies in this box were calculated for every day of tracking. The ratio of OLR and LHF anomalies to precipitation anomalies (converted to W m^{-2} using latent heat of vaporization) was then calculated and composited at each longitude for both persisting and terminating events and plotted in Fig. 6. Because the precipitation

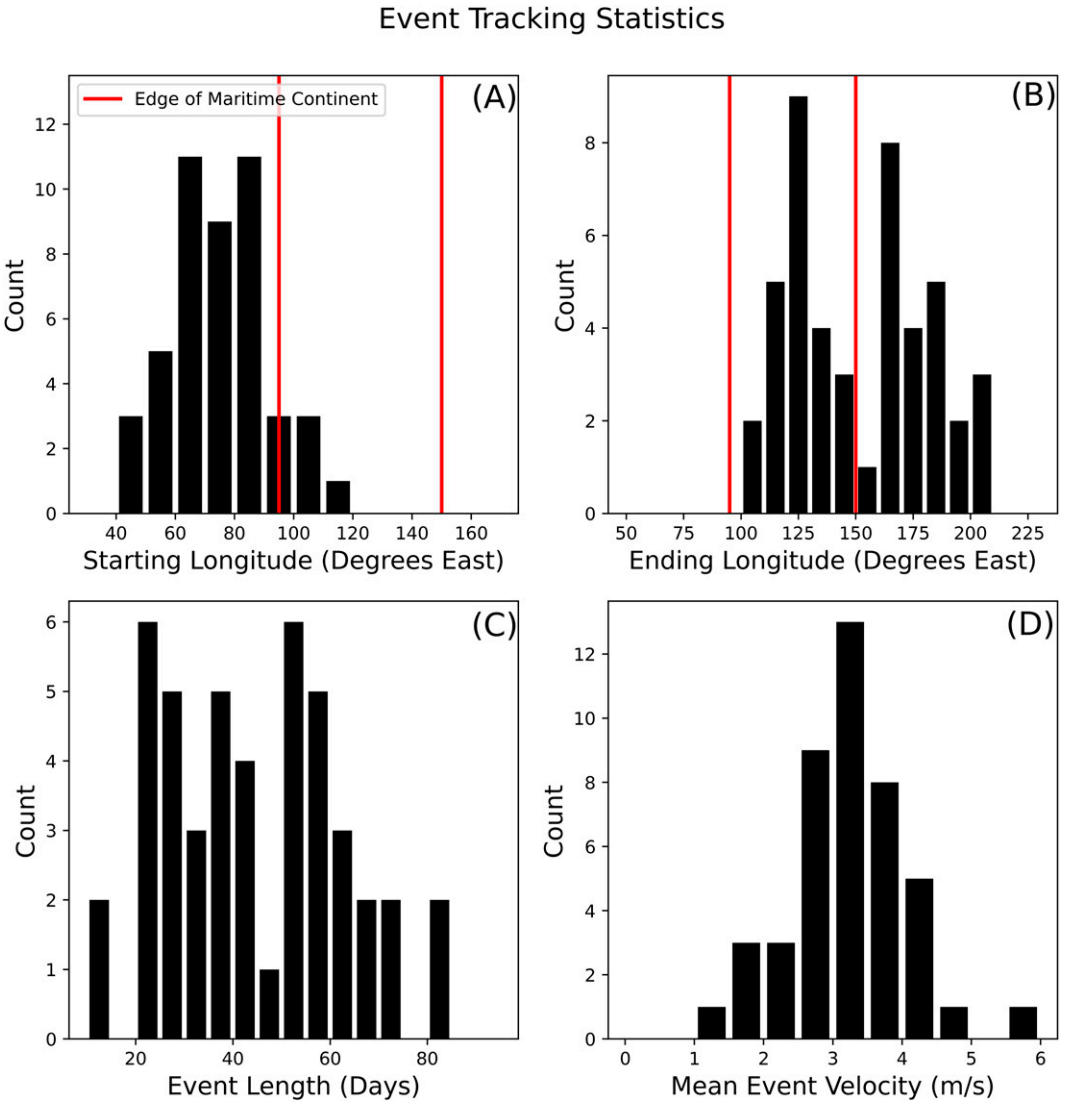

FIG. 4. Distributions of where our algorithm (a) began tracking MJO events and (b) ceased tracking MJO events, (c) how long each MJO event was tracked, and (d) the mean propagation speed of each MJO event. A clear bimodal distribution can be seen in (b), which we use to divide MJO events into persisting and terminating categories.

dataset we use is more limited in time than that for LHF and OLR, we limited this analysis to only the events that occurred from 2001 to 2020.

Figure 6 indicates that LHF anomalies are not necessarily locally more important per unit precipitation anomaly for propagating versus terminating events. In fact, terminating events have slightly higher normalized LHF anomalies in the MC region (0.110 for persisting events and 0.126 for terminating events), and fluxes for terminating events become even more important when viewed relative to OLR anomalies which decrease per unit precipitation for terminating events. However, the centroid-relative composites below tell a more nuanced picture.

Maps of LHF, SST, and precipitation anomalies were composited relative to the convective centroid using the following technique. For every day an event was tracked, a 30° latitude × 100° longitude box centered on the convective feature's geometric centroid was considered. OLR, LHF, SST, wind, and precipitation anomaly values within this box were then averaged across every day of tracking to produce composite spatial distributions of MJO-related variables in latitude and longitude coordinates relative to the centroid.

Figure 7 shows a centroid-centric composite for OAFLUX LHF (colors), OLR (contours), and 850-hPa wind (vectors) anomalies over the entire tracking period for all events, as well as composites separated into persisting and terminating events. For persisting events relative to terminating events, the spatial distribution of both OLR and LHF covers a much larger spatial area with stronger zonal wind anomalies north of the convective center. More extensive regions of significant

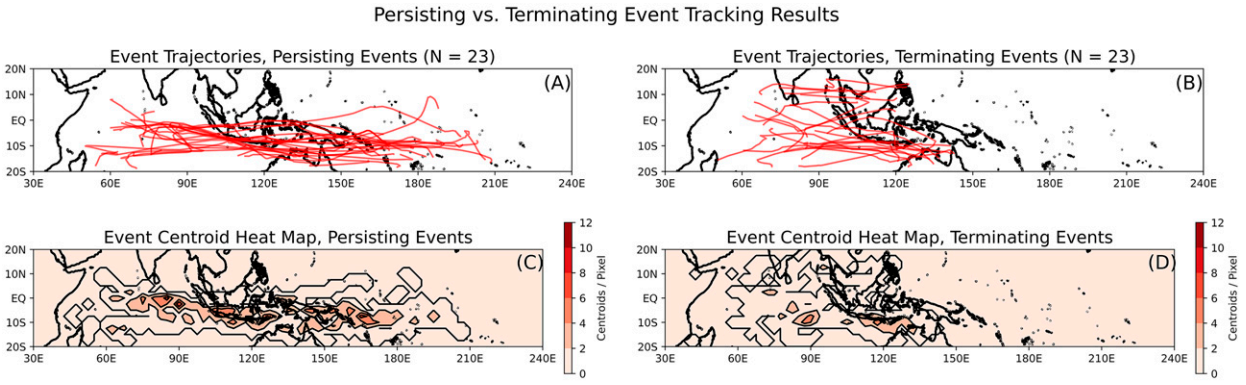

FIG. 5. As in Fig. 2, but for (a),(c) persisting and (b),(d) terminating event categories.

LHF anomalies are found upwind of convection anomalies for persisting events relative to terminating events. A similar significance test of difference between means shows comparable regions of significant differences near and to the west of the convective center (not shown). We note that Wang et al. (2018) showed that climate models with convective events confined to relatively small spatial areas have difficulty propagating the MJO across the MC. The distribution of LHF for persisting events shows a higher spatial coherence with a clear core region that is zonally extended. The LHF distribution for terminating events has no clear core and is oriented in a northwest–southeast fashion.

To help gain more insight into why terminating events end their tracks in the MC region, we examined centroid-centric composites only over the MC region (100°–150°E; Fig. 8). As events progress into the MC region (Fig. 8), persisting events tend to have stronger and more spatially coherent LHF anomalies that span a longer zonal fetch relative to terminating events. As in Fig. 7, more extensive regions of significant LHF anomalies are found upwind of convection anomalies for persisting events relative to terminating events. Given the mean low-level westerly wind and westerly wind anomalies, the effect of these zonally extended flux anomalies would get advected into the convective region. This stronger support by LHF for propagating events would tend to maintain MJO convective anomalies as described in moisture mode theory (e.g., Sobel and Maloney 2013). Over the MC the area of the convective region for persisting events is much greater relative to terminating events. This narrower zonal structure for MJO events that terminate is consistent with that found in

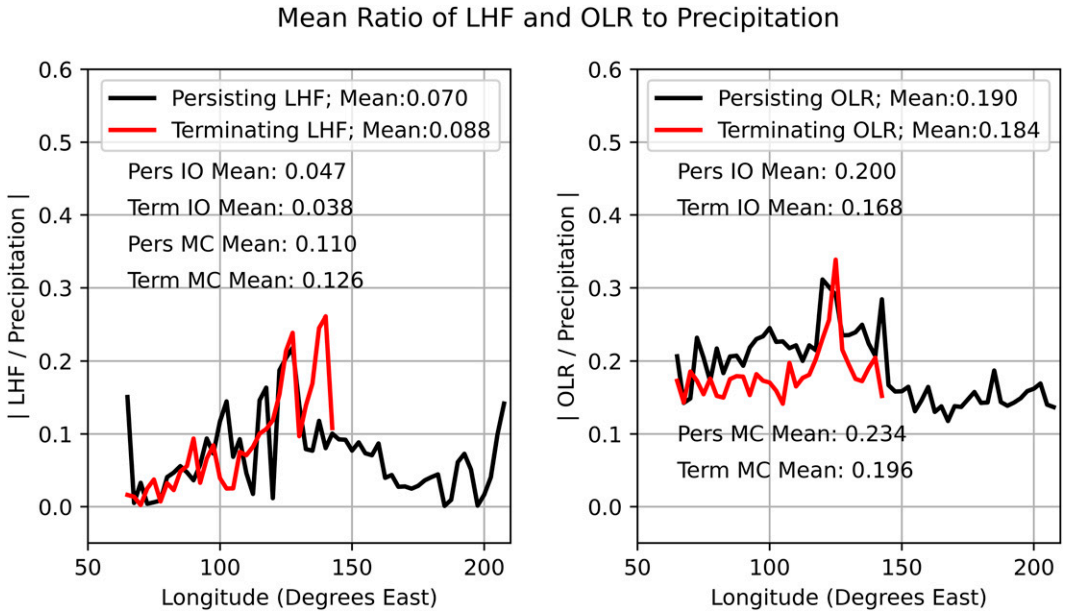

FIG. 6. (a) Ratio of LHF to precipitation anomalies in a 30° longitude × 10° latitude box around tracked event geometric centroids for every day of tracking for both persisting and terminating events. Due to oversensitivity to a small number of days, the first calculated data point for each category was not considered for this analysis. (b) As in (a), but for the ratio of OLR and precipitation anomalies.

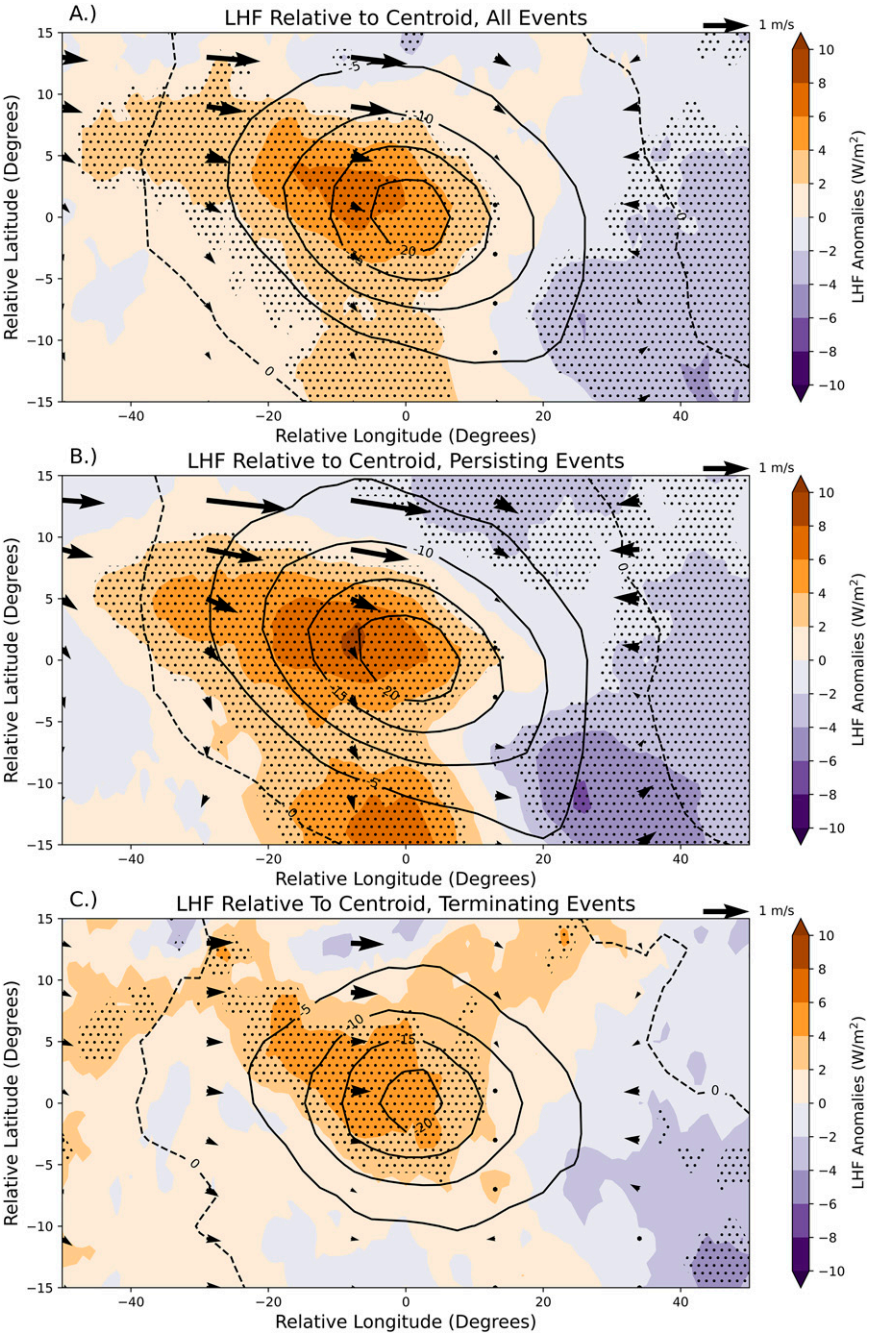

FIG. 7. Composite centroid centric plots of LHF (color) across the entire track for (a) all events, (b) persisting events, and (c) terminating events. Contours are composite OLR anomalies in W m^{-2}. Vectors are 850-hPa wind anomalies. Stippling indicates regions of LHF that are statistically significant at the 95% confidence level based on our bootstrapping experiment.

Wang and Lee (2017), where broader zonal convective structures foster strong Kelvin wave dynamical responses to the east of MJO convection that foster propagation. It is also possible that the smaller spatial scale of convection anomalies for terminating events suppresses radiative feedbacks (e.g., Adames and Kim 2016), which is also supported by Fig. 6. Persisting events also show stronger 850-hPa wind anomalies across the region than terminating events.

In summary, over the lifetime of tracked events LHF appears to provide more energy in regions of MJO convective anomalies for persisting events versus terminating events, and over a larger fetch that is comparable in size to the core

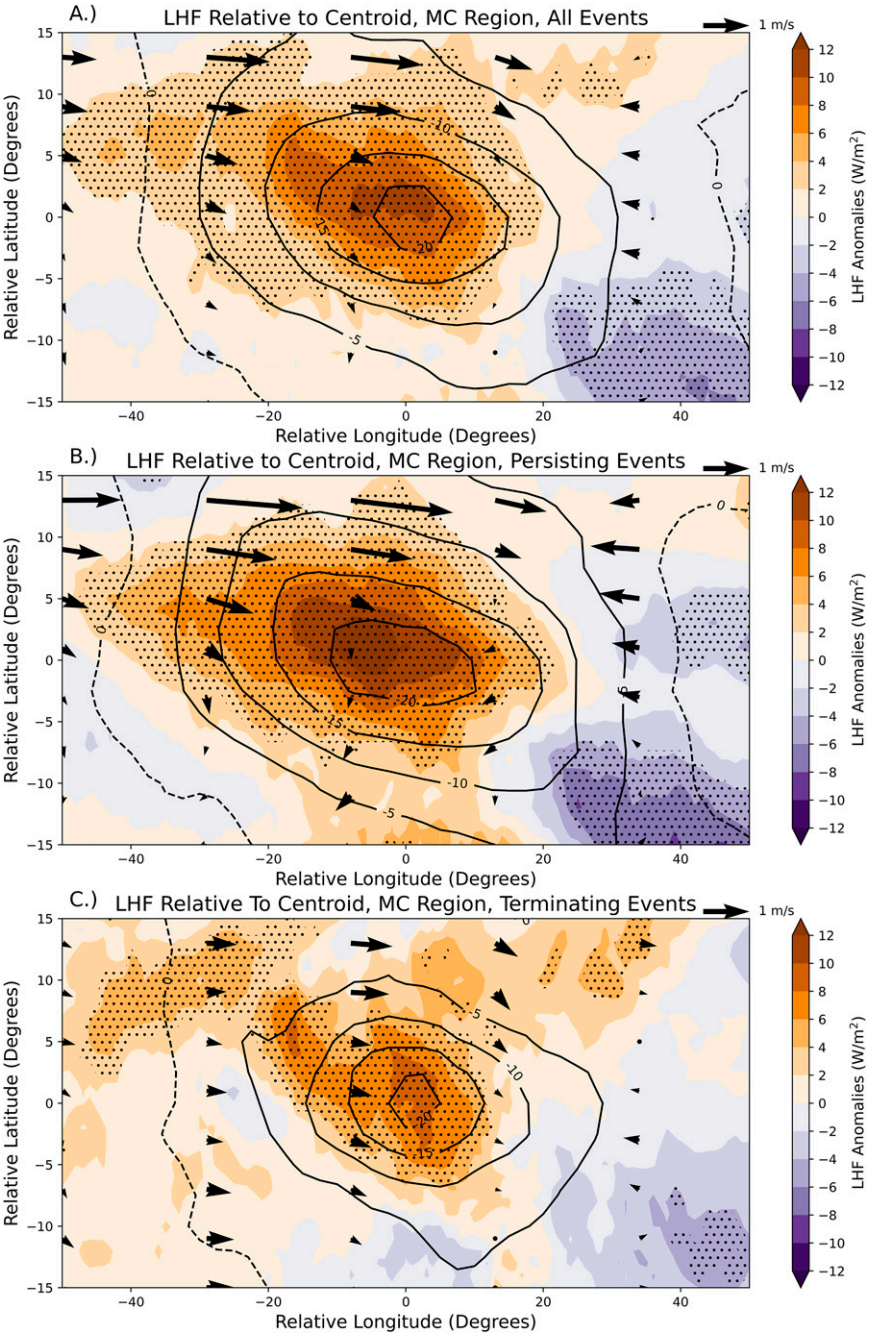

FIG. 8. As in Fig. 7, butt for just over the MC region 100°–150°E. Stippling indicates regions of LHF that are statistically significant at the 95% confidence level based on our bootstrapping experiment.

region of convection. These characteristics are even more accentuated for persisting events in the MC region. Hence, local LHF enhancement may play an important role in helping to provide energy and moisture to the MJO that helps events overcome the "barrier effect" of the MC. Making the assumption that convection is locally supported by moisture as in moisture mode theory (e.g., Adames and Kim 2016), these fluxes may thus help to augment other processes that have been cited as important for propagating the MJO through the MC, including the effects of horizontal moisture advection (e.g., Kim et al. 2014; Ahn et al. 2020).

3) GLOBAL VIEW OF MJO FLUXES DURING PROPAGATING AND TERMINATING EVENTS

Studies such as Raymond and Fuchs (2018) argue that the MJO should be viewed as a global mode in which the MJO

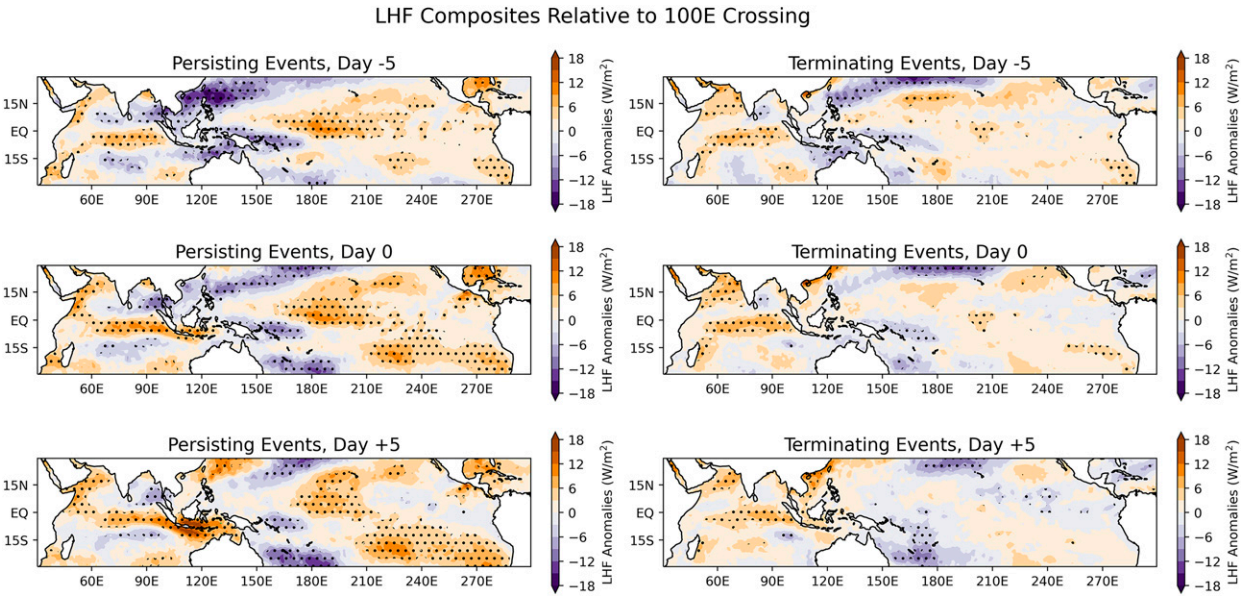

FIG. 9. (left) LHF composites of persisting events at (top) −5, (middle) 0, and (bottom) +5 days relative to the tracked centroid crossing 100°E. (right) As in the left column, but for terminating events. Stippling indicates regions of LHF that are statistically significant at the 95% confidence level based on our bootstrapping experiment.

exists within a regime of low-level zonal mean easterly flow. Easterly MJO anomalies add constructively to this easterly mean flow to produce a wind-driven enhancement of surface fluxes to the east of MJO convection that causes eastward propagation. This view argues that the local processes underpinning the MJO in the Maritime Continent do not exist in a vacuum, and the conditions of the tropics at large can have an impact on MJO propagation through the MC. Hence, this section examines the larger scale factors that potentially impact MJO propagation through the MC.

Given our tracking technique, we can make time-lagged global composite relative to when the MJO centroid crosses a certain location. Figure 9 shows time-lagged global composites of LHF relative to when MJO events propagate across 100°E into the MC region. For the events that tracking initiated east of 100°E, the day tracking initiated was used as day 0. Removing these events did not qualitatively change our results. Looking at the time 5 days before events cross 100°E, persisting events show substantially elevated and widespread statistically significant LHF anomalies across the central and eastern equatorial Pacific and anomalously suppressed LHF over the MC compared to terminating events. At day 0, persisting events continue to show enhanced LHF across the central and eastern equatorial Pacific, and LHF anomalies are modest in that region for terminating events. On day +5, strong positive LHF anomalies associated with persisting events occur near the southern coast of Java, whereas weaker positive flux anomalies with terminating events are found further south near the NW coast of Australia. At this time, the equatorial region of enhanced LHF over the central Pacific Ocean for persisting events begins to transition toward negative LHF anomalies as the MJO convective center propagates into that region (e.g., see Fig. 10). For day −5, 0, and +5 persisting MJO events also show zonal bands of suppressed LHF anomalies at 10°–15°S and 10°–15°N, which potentially help to sharpen the meridional moisture gradient for persisting events.

The large region of enhanced LHF anomalies that occurs near and to the east of the date line for propagating events is a notable signal compared to terminating events, although it is possible that this flux signal could be the remnants of a preceding MJO event that our method did not pick up. To investigate this and further support the potential importance of this central and eastern Pacific flux anomaly for supporting MJO propagation through the Maritime Continent, Hovmöller diagrams of LHF from 10° to 10°S were generated for composites relative to 100°E crossing events (Fig. 10). For persisting events, a strong, statistically significant LHF anomaly is present over the central and eastern equatorial Pacific as the MJO begins to transition into the Maritime Continent, whereas for terminating events it is absent. This LHF feature is relatively stationary, appearing over the equatorial Pacific roughly 15 days before persisting events enter the MC region, and lasts for roughly 25 days. At first glance, the appearance of this LHF anomaly for persisting events is consistent with arguments made in Fuchs and Raymond (2017), Raymond and Fuchs (2018), Sentić et al. (2020) that MJO propagation and dynamics are supported by large-scale enhanced surface fluxes to the east of MJO convection in the presence of mean equatorial easterly flow.

A major question is the extent to which this large-scale flux signal for persisting events is primarily wind-driven, versus having a strong thermodynamic component. To address this question, we begin by examining SST anomalies. Figure 11 is

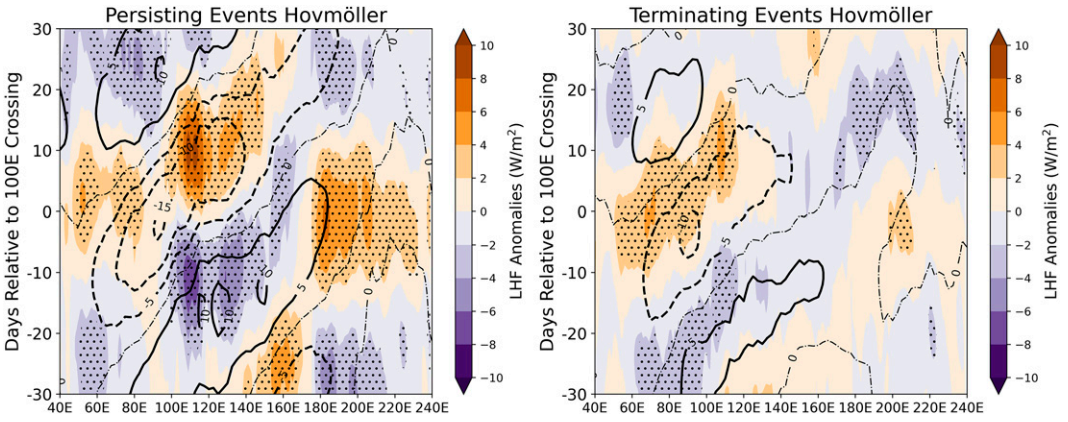

FIG. 10. Composite Hovmöller diagrams of LHF (color) and OLR (contours) anomalies for −30 to +30 days relative to the tracked centroid crossing 100°E. The meridional mean is calculated from 10°N to 10°S. Stippling indicates regions of LHF that are statistically significant at the 95% confidence level based on our bootstrapping experiment.

a composite of SST anomalies relative to the time when MJO events propagate into the MC region, similar to Fig. 9. Persisting events have statistically significant positive SST anomalies greater than 0.1 K over the central and eastern Pacific, which are absent or greatly diminished for terminating events. It is possible the larger SST anomalies near and to the east of the date line for persisting events may contribute to the flux anomaly signal seen in the composites (e.g., Figs. 9, 10). Over the IO and MC regions we also see large coherent signals in SSTs for persisting events which are diminished in both intensity and area for terminating events.

To further investigate potential causes behind this LHF anomaly, we deconstruct LHF anomalies into dynamic and thermodynamic components in three regions of the tropics [Eq. (1)] for the same boxes as in Fig. 3, with an additional box over the peak of the LHF anomaly in the central Pacific (CP box; 10°N–10°S, 180°–200°E). The flux decomposition is conducted as follows:

$$\mathrm{LH}' = \rho L C_H(\overline{\Delta q}|V|' + \Delta q'|\overline{V}|). \quad (1)$$

Here, LH′ represents intraseasonal LHF anomalies, ρ represents density, L is the latent heat of vaporization, and C_H is an exchange coefficient. The $\rho L C_H$ term is represented as an arbitrary scaling factor that is kept constant at a value of 3000 and produces a good fit to the total flux anomaly derived from OAFlux (e.g., see also Maloney and Esbensen 2005). Δq is the difference in specific humidity between the surface of the

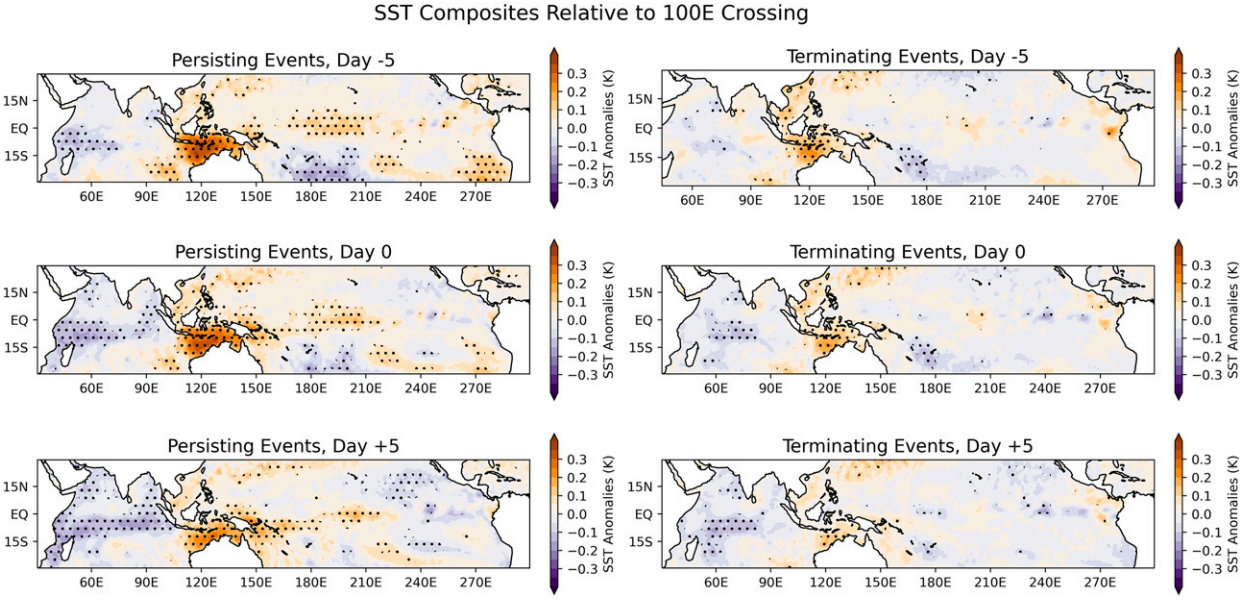

FIG. 11. As in Fig. 9, but for SST anomalies. Stippling indicates regions of SST that are statistically significant at the 95% confidence level based on our bootstrapping experiment.

ocean and 2 m above it, where 2-m specific humidity from OAFlux was used. To calculate ocean surface specific humidity, we assumed that the air at the ocean surface was the same temperature as the OAFlux ocean surface temperature and was fully saturated. $|V|$ represents the magnitude of OAFLUX 10-m winds (the lowest-available level). Primes represent intraseasonally filtered anomalies and overbars represent unfiltered composite means for the duration of each tracked MJO event. A similar decomposition was conducted in Maloney and Esbensen (2005) to examine the influence of thermodynamic versus wind-driven variability in producing east Pacific intraseasonal flux variability during boreal summer.

Figure 12 shows the LHF decomposition of Eq. (1). for all events, persisting events, and terminating events. For the IO Box and the MC Box, wind anomalies primarily drive the LHF anomaly, which agrees well with previous results for the MJO in these regions (DeMott et al. 2014, 2016; Riley Dellaripa and Maloney 2015). In the CP Box, for persisting events the LHF anomaly is of a similar magnitude as for the IO Box, although the LHF anomaly is driven approximately equally by a mixture of thermodynamic and dynamic components. This differs from the WISHE model of Raymond and Fuchs (2018), where the flux anomaly to the east of MJO convection was primarily wind-driven. This also differs from the modeling work of DeMott et al. (2014) that places the thermodynamic-driven component of MJO-related LHF over the date line at less than 20%. For terminating events, the LHF anomaly in the CP box is greatly reduced and is driven almost entirely by thermodynamic effects.

b. CYGNSS results

Utilizing reflected Global Positioning System (GPS) signals off the ocean surface, CYGNSS retrieves ocean surface roughness to estimate surface winds and, with complementary reanalysis estimates of near-surface temperatures and humidity, latent heat flux. This allows CYGNSS to provide high-quality hourly coverage of wind speed and fluxes for swaths of the tropical oceans. Because CYGNSS launched in late 2016 and scientific quality data began in 2018, the time span to study MJO events since the beginning of the CYGNSS region, while growing, is limited. However, we use the CYGNSS output that is available to provide a comparison to OAFLUX-derived results. To increase the number of events over the CYGNSS record we relaxed our size condition for tracking from 62.5 to 31.25 deg^2, which is similar to the size threshold of Kerns and Chen (2016).

For the three boreal winters beginning in 2018, 2019, and 2020, our settings yielded four tracked events, of which three were classified as persisting, and one was terminating. Figure 13a shows the trajectories of the four CYGNSS events with a 5-day simple moving average applied to the tracks, and composite CDR v1.1 LHF and SDR v3.1 surface winds on day 0 are shown in Fig. 13b. As in Figs. 2 and 4, the tracks are smoothed using a simple 5-day moving average. Three of the events detoured south of the MC region, and one event initiated to the north of the MC and dissipated around 160°E. Because the sample size is too limited for meaningful composites, we looked at each individual event on day 0 relative to its crossing of 100°E.

While an elevated surface flux anomaly contributed by both wind speed and thermodynamic contributions was present in the central Pacific for the three persisting events, we identified during the CYGNSS period, consistent with previous results, the small sample size prevents any robust conclusions, especially when compared with the terminating event.

c. Global mean wind

In the work of Fuchs and Raymond (2017), Raymond and Fuchs (2018), and Sentić et al. (2020) an easterly low-level zonal mean wind in the tropics plays a key role in producing LHF anomalies that aid MJO propagation through WISHE. A possibility is that stronger mean easterly flow during propagating events may support MJO propagation. Using the record of 1000-hPa zonal wind provided by ERA5 we looked at the patterns of low-level zonal wind averaged from 10°N to 10°S from 1979 to 2020 across the tropics for propagating versus terminating events.

Figure 14a presents daily mean zonal mean zonal wind averaged between 10°N and 10°S from 1979 to 2020. The mean zonal wind across the entire year is easterly and is at its strongest during the period we defined "boreal winter," December–April, in particular, which is also when MJO amplitude maximizes. Figure 14b shows how the low-level background wind differs between persisting and terminating events. To do this, a mean of the total 1000-hPa zonal wind from 10°N to 10°S at each longitude was constructed for every day of tracking for both persisting and terminating events. Over the Indian Ocean region (50°–100°E), terminating events have a background zonal mean westerly wind approximately 1 m s^{-1} stronger than that of persisting events between 10°N and 10°S, with the differences statistically significant at the 95% level using a two-tailed t test. Over the Pacific Ocean from 150° to 215°E, terminating events have a stronger easterly flow of 0.4 m s^{-1} across the entire region compared to persisting events. The differences of the winds between propagating and terminating events at 150°–215°E are statistically significant at the 95% level. When Fig. 14b is averaged across the entire tropics, this results in a mean zonal wind of −2.49 m s^{-1} for persisting events, and −2.47 m s^{-1} for terminating events. Hence, it appears that stronger mean easterly flow is not supporting propagation during persisting events.

4. Discussion

The results of section 3 are used to test the importance of surface flux feedbacks to the MJO in the context of two major theories for MJO dynamics, moisture mode theory (e.g., Sobel and Maloney 2012, 2013), and WISHE (e.g., Raymond and Fuchs 2018). This study joins the body of recent theoretical, observational, and modeling studies that have sought to understand the role of LHF in MJO maintenance and propagation (Bui et al. 2020; DeMott et al. 2014, 2015; Emanuel 2020; Fuchs and Raymond 2017; Khairoutdinov and Emanuel 2018; Maloney 2009; Raymond and Fuchs 2018; Riley Dellaripa and Maloney 2015; Sentić et al. 2020; Sobel and Maloney 2012;

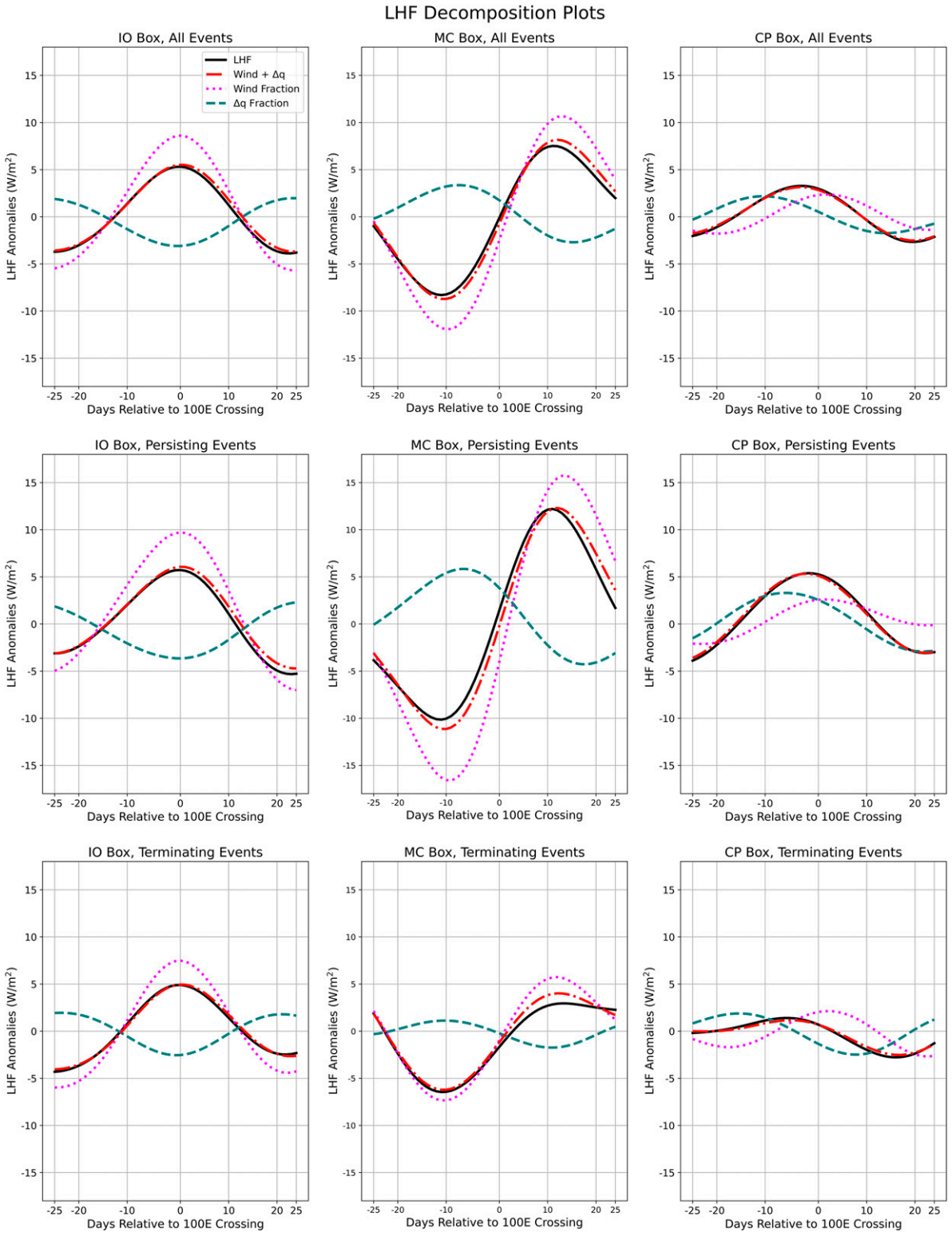

FIG. 12. LHF decomposition across composite event lifetimes for the three regions used in Fig. 3 for (top) all events, (middle) persisting events, and (bottom) terminating events.

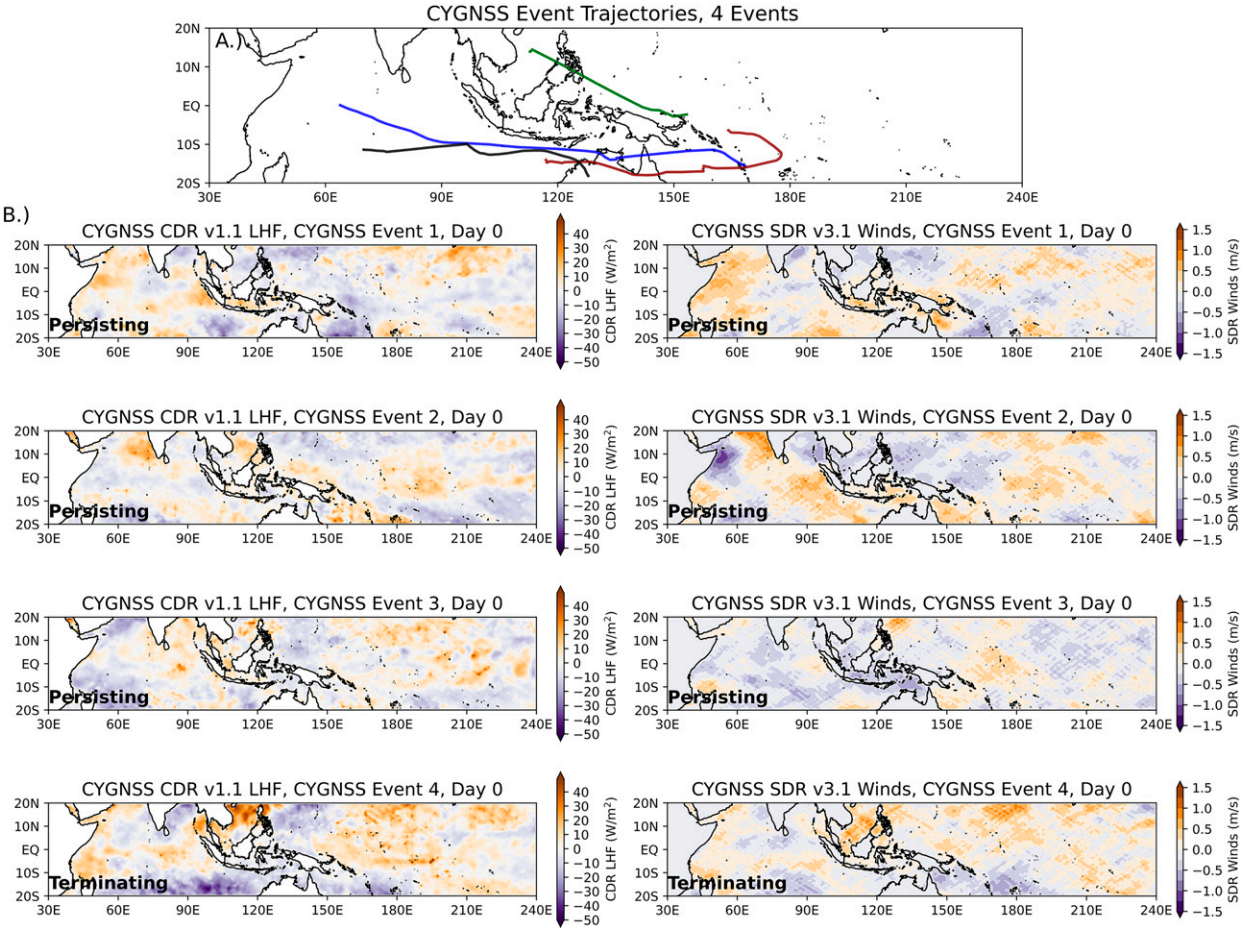

FIG. 13. (a) CYGNSS tracks at day 0 relative to the 100°E crossing and (b) LHF and surface wind speed anomaly composites for the four CYGNSS events.

Wolding and Maloney 2015). Regarding WISHE theory, in section 3 we showed that there is a quasi-stationary positive intraseasonal LHF anomaly over the equatorial Pacific Ocean centered around 180°–200°E that is present for events that persist through the MC region and absent for those that terminate over that region. WISHE theories to explain MJO propagation produce results that agree with our observations, at least in terms of the presence of this latent heat flux signal. However,

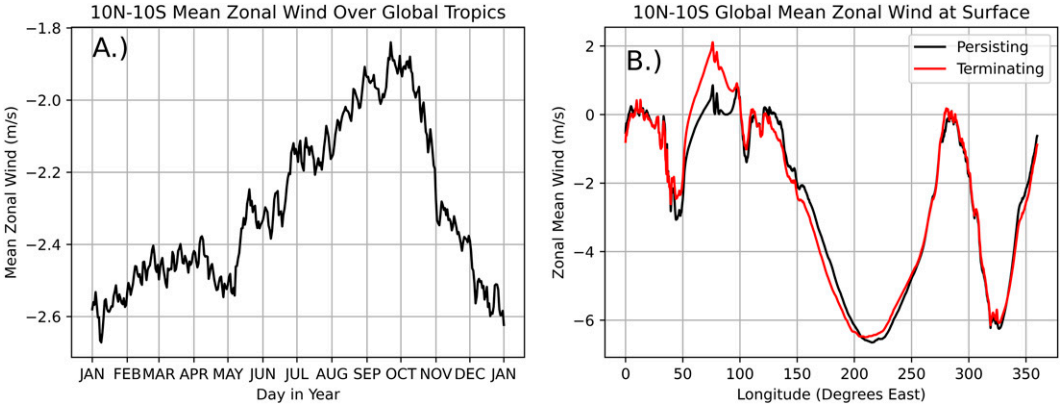

FIG. 14. (a) Daily mean zonal-mean zonal wind at 1000 hPa between 10°N and 10°S from ERA5 from 1979 to 2020. (b) Composite zonal wind averaged from 10°N to 10°S on days where our algorithm tracked persisting events (black) and terminating events (red).

the enhanced fluxes that contribute to the production of moisture east of the MJO are not entirely wind-driven in our observations, and this does represent a discrepancy between our results and recent theory.

Sentić et al. (2020) expounds upon the ideas presented in Fuchs and Raymond (2017) and Raymond and Fuchs (2018) by examining a composite MJO event from reanalysis. In their analysis, they found that there is a large, slow-moving positive LHF anomaly to the east of the center of MJO convection. This is similar to the phenomena we identified in our study that is centered around 180°–200°E. The flux feature in their study is associated with a moistening of the boundary layer, although their observed LHF anomalies are slightly displaced in space and time relative to the boundary layer moistening, with the moistening signal occurring west of the LHF anomaly and east of the center of MJO convection.

Arnold and Randall (2015) and Khairoutdinov and Emanuel (2018) present a convective self-aggregation model in zonally symmetric aquaplanet simulations with mean easterly winds across the tropics of an MJO-like disturbance that produces similar features to our observed events. Both studies produce a peak in surface fluxes and moisture advection to the east of MJO convection that roughly aligns with where our observations place the LHF anomaly.

A similar purely wind-driven LHF anomaly is present in the model of Raymond and Fuchs (2018), where the leading LHF anomaly serves to increase tropospheric moisture, supporting propagation of MJO convection into that region. Our results show that the leading LHF anomaly over the equatorial Pacific is driven equally by dynamic and thermodynamic effects. If this flux anomaly over the Central Pacific is essential to MJO propagation, it suggests that an entirely wind-driven theory for LHF propagation may be insufficient and some thermodynamic mechanism could be needed to complete the explanation. We also show that our observed LHF anomaly over the Pacific does not have a noticeable phase speed in a Hovmöller composite. This suggests that the driver of this anomaly differs in detail from that in papers like Raymond and Fuchs (2018) where the latent heat flux anomaly to the east of MJO convection propagates eastward more continuously and is wind-driven. The fast MJO circulation propagation away from the west Pacific that imposes same-signed wind anomalies across the east Pacific may rapidly impose this feature (e.g., Rydbeck et al. 2013). In particular, a potential driver of the leading SST anomalies that contributes thermodynamically to the LHF anomaly is an extensive quasi-stationary region of MJO westerly wind anomalies produced by the leading region of suppressed convection over the west Pacific Ocean. This quasi-stationary region reduces the mean easterlies, wind speed, and upwelling in the central and east Pacific region (Maloney and Hartmann 1998). Reducing both the wind-driven evaporation over the region and the cooling due to upwelling, resulting in a positive SST anomaly that contributes thermodynamically to flux anomalies. Future work is necessary, including an analysis of the upper ocean heat budget, to confirm this.

The work of Ahn et al. (2020) and Kang et al. (2020) highlights how improved mean-state moisture gradients, particularly meridional moisture gradients, promotes better MJO propagation through the MC. They cite weakened moisture gradients during La Niña conditions as favoring termination of MJO events in the Maritime Continent region. While the stronger average mean zonal winds in the central Pacific in our terminating events are consistent with a La Niña–like state, we find no notable relationship between our propagating and terminating events and ENSO state.

5. Conclusions

A new algorithm is presented that is capable of identifying and tracking MJO events using 30–96-day bandpass filtered OLR anomalies. This technique was applied to track MJO events using NOAA interpolated OLR anomalies from 1985 to 2020. The role of surface latent heat fluxes both locally and globally in MJO propagation and maintenance was investigated using this algorithm. Forty-six MJO events were identified, and half of them fail to propagate through the MC region. Most events, whether they terminate over the MC or not, detour to the south of the MC, which agrees with previous observational results. Persisting events have stronger and more coherent LHF anomalies with a longer zonal fetch in the vicinity of the convective center compared to terminating events. This behavior is particularly pronounced when the MJO is located in the MC region, and would tend to support MJO propagation through the region as view through moisture mode theory (e.g., Maloney 2009). Terminating events also tend to be smaller in scale, consistent with previous results in the literature indicating that MJO events with larger spatial scales are better able to propagate eastward (e.g., Wang and Lee 2017).

Events that propagate through the MC also exhibit a large stationary region of positive LHF anomalies over the central and eastern equatorial Pacific that is absent for terminating events. While the presence of this feature is broadly consistent with modern theories of MJO propagation involving WISHE, it is stationary and has a large thermodynamic component in addition to a wind-driven component, making the details different from that predicted in the work of Fuchs and Raymond (2017) and Raymond and Fuchs (2018). Modifications to WISHE theory that account for a thermodynamic component to LHF anomalies may be needed to fully understand how MJO events overcome the "barrier effect" of the MC.

Future work will focus on investigating the mechanisms responsible for formation of the region of high LHF across the central equatorial Pacific that accompanies persisting events, the intensity and possible importance of moisture advection from the anomalous Pacific Ocean LHF region toward the MJO convective center, and comparing global wind anomalies for propagating and terminating events to diagnose the different nature of dynamical signals associated with the spatially larger convective anomalies for persisting events. As more CYGNSS data becomes available, it will also be possible to examine LHF anomalies for future MJO events in enhanced detail, possibly providing more clues into how LHF impacts MJO propagation.

Acknowledgments. This work was funded by the NOAA CVP program under grant NA18OAR4310299, and by NASA CYGNSS Grant 80NSSC21K1004.

Data availability statement. All data used in this study is publicly available online. A Python script for the tracking algorithm is available upon request and will be made available via GitHub.

REFERENCES

Adames, Á. F., and D. Kim, 2016: The MJO as a dispersive, convectively coupled moisture wave: Theory and observations. *J. Atmos. Sci.*, **73**, 913–941, https://doi.org/10.1175/JAS-D-15-0170.1.

Ahn, M., and Coauthors, 2020: MJO propagation across the Maritime Continent: Are CMIP6 models better than CMIP5 models? *Geophys. Res. Lett.*, **47**, e2020GL087250, https://doi.org/10.1029/2020GL087250.

Araligidad, N. M., and E. D. Maloney, 2008: Wind-driven latent heat flux and the intraseasonal oscillation. *Geophys. Res. Lett.*, **35**, L04815, https://doi.org/10.1029/2007GL032746.

Arcodia, M. C., B. P. Kirtman, and L. S. P. Siqueira, 2020: How MJO teleconnections and ENSO interference impacts U.S. precipitation. *J. Climate*, **33**, 4621–4640, https://doi.org/10.1175/JCLI-D-19-0448.1.

Arnold, N. P., and D. A. Randall, 2015: Global-scale convective aggregation: Implications for the Madden–Julian oscillation. *J. Adv. Model. Earth Syst.*, **7**, 1499–1518, https://doi.org/10.1002/2015MS000498.

Baggett, C. F., E. A. Barnes, E. D. Maloney, and B. D. Mundhenk, 2017: Advancing atmospheric river forecasts into subseasonal-to-seasonal time scales. *Geophys. Res. Lett.*, **44**, 7528–7536, https://doi.org/10.1002/2017GL074434.

Barnes, E. A., S. M. Samarasinghe, I. Ebert-Uphoff, and J. C. Furtado, 2019: Tropospheric and stratospheric causal pathways between the MJO and NAO. *J. Geophys. Res. Atmos.*, **124**, 9356–9371, https://doi.org/10.1029/2019JD031024.

Bui, H. X., E. D. Maloney, E. M. Riley Dellaripa, and B. Singh, 2020: Wind speed, surface flux, and intraseasonal convection coupling from CYGNSS data. *Geophys. Res. Lett.*, **47**, e2020GL090376, https://doi.org/10.1029/2020GL090376.

CLIVAR Madden–Julian Oscillation Working Group, 2009: MJO simulation diagnostics. *J. Climate*, **22**, 3006–3030, https://doi.org/10.1175/2008JCLI2731.1.

Copernicus Climate Change Service (C3S), 2017: ERA5: Fifth generation of ECMWF atmospheric reanalyses of the global climate. Copernicus Climate Change Service Climate Data Store, accessed 27 January 2022, https://cds.climate.copernicus.eu/cdsapp#!/home.

Crespo, J. A., D. J. Posselt, and S. Asharaf, 2019: CYGNSS surface heat flux product development. *Remote Sens.*, **11**, 2294, https://doi.org/10.3390/rs11192294.

DeMott, C. A., C. Stan, D. A. Randall, and M. D. Branson, 2014: Intraseasonal variability in coupled GCMs: The roles of ocean feedbacks and model physics. *J. Climate*, **27**, 4970–4995, https://doi.org/10.1175/JCLI-D-13-00760.1.

——, N. P. Klingaman, and S. J. Woolnough, 2015: Atmosphere-ocean coupled processes in the Madden–Julian oscillation. *Rev. Geophys.*, **53**, 1099–1154, https://doi.org/10.1002/2014RG000478.

——, J. J. Benedict, N. P. Klingaman, S. J. Woolnough, and D. A. Randall, 2016: Diagnosing ocean feedbacks to the MJO: SST-modulated surface fluxes and the moist static energy budget. *J. Geophys. Res. Atmos.*, **121**, 8350–8373, https://doi.org/10.1002/2016JD025098.

——, B. O. Wolding, E. D. Maloney, and D. A. Randall, 2018: Atmospheric mechanisms for MJO decay over the Maritime Continent. *J. Geophys. Res. Atmos.*, **123**, 5188–5204, https://doi.org/10.1029/2017JD026979.

Emanuel, K. A., 1987: An air–sea interaction model of intraseasonal oscillations in the tropics. *J. Atmos. Sci.*, **44**, 2324–2340, https://doi.org/10.1175/1520-0469(1987)044,2324:AASIMO.2.0.CO;2.

——, 2020: Slow modes of the equatorial waveguide. *J. Atmos. Sci.*, **77**, 1575–1582, https://doi.org/10.1175/JAS-D-19- 0281.1.

Fuchs, Ž., and D. J. Raymond, 2017: A simple model of intraseasonal oscillations. *J. Adv. Model. Earth Syst.*, **9**, 1195–1211, https://doi.org/10.1002/2017MS000963.

Gleason, S., M. M. Al-Khaldi, C. S. Ruf, D. S. McKague, T. Wang, and A. Russel, 2022: Characterizing and mitigating digital sampling effects on the CYGNSS level 1 calibration. *IEEE Trans. Geosci. Remote Sens.*, **60**, 5802812, https://doi.org/10.1109/TGRS.2021.3120026.

Gonzalez, A. O., and X. Jiang, 2019: Distinct propagation characteristics of intraseasonal variability over the tropical West Pacific. *J. Geophys. Res. Atmos.*, **124**, 5332–5351, https://doi.org/10.1029/2018JD029884.

Guan, B., and D. E. Waliser, 2015: Detection of atmospheric rivers: Evaluation and application of an algorithm for global studies: Detection of atmospheric rivers. *J. Geophys. Res. Atmos.*, **120**, 12 514–12 535, https://doi.org/10.1002/2015JD024257.

Henderson, S. A., E. D. Maloney, and E. A. Barnes, 2016: The influence of the Madden–Julian oscillation on Northern Hemisphere winter blocking. *J. Climate*, **29**, 4597–4616, https://doi.org/10.1175/JCLI-D-15-0502.1.

Hersbach, H., and Coauthors, 2020: The ERA5 global reanalysis. *Quart. J. Roy. Meteor. Soc.*, **146**, 1999–2049, https://doi.org/10.1002/qj.3803.

Hirata, F. E., P. J. Webster, and V. E. Toma, 2013: Distinct manifestations of austral summer tropical intraseasonal oscillations. *Geophys. Res. Lett.*, **40**, 3337–3341, https://doi.org/10.1002/grl.50632.

Hsiao, W.-T., E. A. Barnes, E. D. Maloney, S. N. Tulich, J. Dias, and G. N. Kiladis, 2022: Role of the tropics in state-dependent improvements of US West Coast NOAA unified forecast system precipitation forecasts. *Geophys. Res. Lett.*, **49**, e2021GL096447, https://doi.org/10.1029/2021GL096447.

Huffman, G. J., E. F. Stocker, D. T. Bolvin, E. J. Nelkin, and J. Tan, 2019: GPM IMERG final precipitation L3 1 day 0.1 degree × 0.1 degree V06 (GPM_3IMERGDF). NASA Goddard Earth Sciences Data and Information Services Center, accessed 26 January 2021, https://doi.org/10.5067/GPM/IMERGDF/DAY/06.

Inness, P. M., and J. M. Slingo, 2006: The interaction of the Madden–Julian oscillation with the Maritime Continent in a GCM. *Quart. J. Roy. Meteor. Soc.*, **132**, 1645–1667, https://doi.org/10.1256/qj.05.102.

Jiang, X., and Coauthors, 2020: Fifty years of research on the Madden-Julian Oscillation: Recent progress, challenges, and perspectives. *J. Geophys. Res. Atmos.*, **125**, e2019JD030911, https://doi.org/10.1029/2019JD030911.

Jones, P. W., 1999: First- and second-order conservative remapping schemes for grids in spherical coordinates. *Mon. Wea. Rev.*, **127**, 2204–2210, https://doi.org/10.1175/1520-0493(1999)127<2204:FASOCR>2.0.CO;2.

Kang, D., D. Kim, M.-S. Ahn, R. Neale, J. Lee, and P. J. Gleckler, 2020: The role of the mean state on MJO simulation in

CESM2 ensemble simulation. *Geophys. Res. Lett.*, **47**, e2020GL089824, https://doi.org/10.1029/2020GL089824.

——, ——, S. Rushley, and E. D. Maloney, 2022: Seasonal locking of the MJO's southward detouring of the Maritime Continent: The role of the Australian monsoon. *J. Climate*, **35**, 4553–4568, https://doi.org/10.1175/JCLI-D-22-0234.1.

Kerns, B. W., and S. S. Chen, 2016: Large-scale precipitation tracking and the MJO over the Maritime Continent and Indo-Pacific warm pool. *J. Geophys. Res. Atmos.*, **121**, 8755–8776, https://doi.org/10.1002/2015JD024661.

——, and ——, 2020: A 20-year climatology of Madden-Julian Oscillation convection: Large-scale precipitation tracking from TRMM-GPM rainfall. *J. Geophys. Res. Atmos.*, **125**, e2019JD032142, https://doi.org/10.1029/2019JD032142.

Khairoutdinov, M. F., and K. Emanuel, 2018: Intraseasonal variability in a cloud-permitting near-global equatorial aquaplanet model. *J. Atmos. Sci.*, **75**, 4337–4355, https://doi.org/10.1175/JAS-D-18-0152.1.

Kiladis, G. N., J. Dias, K. H. Straub, M. C. Wheeler, S. N. Tulich, K. Kikuchi, K. M. Weickmann, and M. J. Ventrice, 2014: A comparison of OLR and circulation-based indices for tracking the MJO. *Mon. Wea. Rev.*, **142**, 1697–1715, https://doi.org/10.1175/MWR-D-13-00301.1.

Kim, D., J.-S. Kug, and A. H. Sobel, 2014: Propagating versus nonpropagating Madden–Julian Oscillation events. *J. Climate*, **27**, 111–125, https://doi.org/10.1175/JCLI-D-13-00084.1.

Lee, H.-J., and K.-H. Seo, 2019: Impact of the Madden-Julian oscillation on Antarctic sea ice and its dynamical mechanism. *Sci. Rep.*, **9**, 10761, https://doi.org/10.1038/s41598-019-47150-3.

Liebmann, B., and C. A. Smith, 1996: Description of a complete (interpolated) outgoing longwave radiation dataset. *Bull. Amer. Meteor. Soc.*, **77**, 1275–1277.

Ling, J., C. Zhang, R. Joyce, P. Xie, and G. Chen, 2019: Possible role of the diurnal cycle in land convection in the barrier effect on the MJO by the Maritime Continent. *Geophys. Res. Lett.*, **46**, 3001–3011, https://doi.org/10.1029/2019GL081962.

Madden, R. A., and P. R. Julian, 1971: Detection of a 40–50 day oscillation in the zonal wind in the tropical Pacific. *J. Atmos. Sci.*, **28**, 702–708, https://doi.org/10.1175/1520-0469(1971)028<0702:DOADOI>2.0.CO;2.

——, and ——, 1972: Description of global-scale circulation cells in the tropics with a 40–50 day period. *J. Atmos. Sci.*, **29**, 1109–1123, https://doi.org/10.1175/1520-0469(1972)029<1109:DOGSCC>2.0.CO;2.

Maloney, E. D., 2009: The moist static energy budget of a composite tropical intraseasonal oscillation in a climate model. *J. Climate*, **22**, 711–729, https://doi.org/10.1175/2008JCLI2542.1.

——, and D. L. Hartmann, 1998: Frictional moisture convergence in a composite life cycle of the Madden–Julian oscillation. *J. Climate*, **11**, 2387–2403, https://doi.org/10.1175/1520-0442(1998)011<2387:FMCIAC>2.0.CO;2.

——, and ——, 2000: Modulation of eastern North Pacific hurricanes by the Madden–Julian oscillation. *J. Climate*, **13**, 1451–1460, https://doi.org/10.1175/1520-0442(2000)013<1451:MOENPH>2.0.CO;2.

——, and A. H. Sobel, 2004: Surface fluxes and ocean coupling in the tropical intraseasonal oscillation. *J. Climate*, **17**, 4368–4386, https://doi.org/10.1175/JCLI-3212.1.

——, and S. K. Esbensen, 2005: A modeling study of summertime East Pacific wind-induced ocean–atmosphere exchange in the intraseasonal oscillation. *J. Climate*, **18**, 568–584, https://doi.org/10.1175/JCLI-3280.1.

McPhaden, M. J., 1999: Genesis and evolution of the 1997–98 El Niño. *Science*, **283**, 950–954, https://doi.org/10.1126/science.283.5404.950.

Nardi, K. M., C. F. Baggett, E. A. Barnes, E. D. Maloney, D. S. Harnos, and L. M. Ciasto, 2020: Skillful all-season S2S prediction of U.S. precipitation using the MJO and QBO. *Wea. Forecasting*, **35**, 2179–2198, https://doi.org/10.1175/WAF-D-19-0232.1.

Pascual, D., M. P. Clarizia, and C. S. Ruf, 2021: Improved CYGNSS wind speed retrieval using significant wave height correction. *Remote Sens.*, **13**, 4313, https://doi.org/10.3390/rs13214313.

Raymond, D. J., and Ž. Fuchs, 2018: The Madden-Julian Oscillation and the Indo-Pacific warm pool. *J. Adv. Model. Earth Syst.*, **10**, 951–960, https://doi.org/10.1002/2017MS001258.

Riley Dellaripa, E. M., and E. D. Maloney, 2015: Analysis of MJO wind-flux feedbacks in the Indian Ocean using RAMA buoy observations. *J. Meteor. Soc. Japan*, **93A**, 1–20, https://doi.org/10.2151/jmsj.2015-021.

Ruf, C. S., 2018: Cyclone Global Navigation Satellite System (CYGNSS). Algorithm Theoretical Basis Document Level 3 Gridded Wind Speed, CYGNSS, 10 pp., https://cygnss.engin.umich.edu/wp-content/uploads/sites/534/2021/07/148-0319-ATBD-L3-Gridded-Wind-Speed_Rev1_Aug2018_release.pdf.

——, and Coauthors, 2016: New ocean winds satellite mission to probe hurricanes and tropical convection. *Bull. Amer. Meteor. Soc.*, **97**, 385–395, https://doi.org/10.1175/BAMS-D-14-00218.1.

——, S. Asharaf, R. Balasubramaniam, S. Gleason, T. Lang, D. McKague, D. Twigg, and D. Waliser, 2019: In-orbit performance of the constellation of CYGNSS hurricane satellites. *Bull. Amer. Meteor. Soc.*, **100**, 2009–2023, https://doi.org/10.1175/BAMS-D-18-0337.1.

Rydbeck, A. V., E. D. Maloney, S.-P. Xie, J. Hafner, and J. Shaman, 2013: Remote forcing versus local feedback of East Pacific intraseasonal variability during boreal summer. *J. Climate*, **26**, 3575–3596, https://doi.org/10.1175/JCLI-D-12-00499.1.

Salby, M. L., and H. H. Hendon, 1994: Intraseasonal behavior of clouds, temperature, and motion in the tropics. *J. Atmos. Sci.*, **51**, 2207–2224, https://doi.org/10.1175/1520-0469(1994)051<2207:IBOCTA>2.0.CO;2.

Sentić, S., Ž. Fuchs-Stone, and D. J. Raymond, 2020: The Madden–Julian Oscillation and mean easterly winds. *J. Geophys. Res. Atmos.*, **125**, e2019JD030869, https://doi.org/10.1029/2019JD030869.

Singh, B., and J. L. Kinter, 2020: Tracking of tropical intraseasonal convective anomalies: 1. Seasonality of the tropical intraseasonal oscillations. *J. Geophys. Res. Atmos.*, **125**, e2019JD030873, https://doi.org/10.1029/2019JD030873.

Sobel, A., and E. Maloney, 2012: An idealized semi-empirical framework for modeling the Madden–Julian Oscillation. *J. Atmos. Sci.*, **69**, 1691–1705, https://doi.org/10.1175/JAS-D-11-0118.1.

——, and ——, 2013: Moisture modes and the eastward propagation of the MJO. *J. Atmos. Sci.*, **70**, 187–192, https://doi.org/10.1175/JAS-D-12-0189.1.

Wang, B., and S.-S. Lee, 2017: MJO propagation shaped by zonal asymmetric structures: Results from 24 GCM simulations. *J. Climate*, **30**, 7933–7952, https://doi.org/10.1175/JCLI-D-16-0873.1.

——, and Coauthors, 2018: Dynamics-oriented diagnostics for the Madden-Julian oscillation. *J. Climate*, 3117–3135, https://doi.org/10.1175/JCLI-D-17-0332.1.

——, G. Chen, and F. Liu, 2019: Diversity of the Madden-Julian Oscillation. *Sci. Adv.*, **5**, eaax0220, https://doi.org/10.1126/sciadv.aax0220.

Wheeler, M., and G. N. Kiladis, 1999: Convectively coupled equatorial waves: Analysis of clouds and temperature in the wavenumber–frequency domain. *J. Atmos. Sci.*, **56**, 374–399, https://doi.org/10.1175/1520-0469(1999)056<0374:CCEWAO>2.0.CO;2.

——, and H. H. Hendon, 2004: An all-season real-time multivariate MJO Index: Development of an index for monitoring and prediction. *Mon. Wea. Rev.*, **132**, 1917–1932, https://doi.org/10.1175/1520-0493(2004)132<1917:AARMMI>2.0.CO;2.

Wolding, B. O., and E. D. Maloney, 2015: Objective diagnostics and the Madden–Julian oscillation. Part II: Application to moist static energy and moisture budgets. *J. Climate*, **28**, 7786–7808, https://doi.org/10.1175/JCLI-D-14-00689.1.

——, ——, and M. Branson, 2016: Vertically resolved weak temperature gradient analysis of the Madden–Julian Oscillation in SP-CESM. *J. Adv. Model. Earth Syst.*, **8**, 1586–1619, https://doi.org/10.1002/2016MS000724.

Wu, C.-H., and H.-H. Hsu, 2009: Topographic influence on the MJO in the Maritime Continent. *J. Climate*, **22**, 5433–5448, https://doi.org/10.1175/2009JCLI2825.1.

Yu, L., and R. A. Weller, 2007: Objectively analyzed air–sea heat fluxes for the global ice-free oceans (1981–2005). *Bull. Amer. Meteor. Soc.*, **88**, 527–540, https://doi.org/10.1175/BAMS-88-4-527.

Zhang, C., 2005: Madden-Julian oscillation. *Rev. Geophys.*, **43**, RG2003, https://doi.org/10.1029/2004RG000158.

——, and J. Ling, 2017: Barrier effect of the Indo-Pacific Maritime Continent on the MJO: Perspectives from tracking MJO precipitation. *J. Climate*, **30**, 3439–3459, https://doi.org/10.1175/JCLI-D-16-0614.1.

Zhou, S., M. L'Heureux, S. Weaver, and A. Kumar, 2012: A composite study of the MJO influence on the surface air temperature and precipitation over the Continental United States. *Climate Dyn.*, **38**, 1459–1471, https://doi.org/10.1007/s00382-011-1001-9.